

Article

Operation of a Modular 3D-Pixelated Liquid Argon Time-Projection Chamber in a Neutrino Beam

S. Abbaslu¹, A. Abed Abud², R. Acciarri³, L. P. Accorsi⁴, M. A. Acero⁵, M. R. Adames⁴, G. Adamov⁶, M. Adamowski³, C. Adriano⁷, F. Akbar⁸, F. Alemanno⁹, N. S. Alex⁸, K. Allison¹⁰, M. Alrashed¹¹, A. Alton¹², R. Alvarez¹³, T. Alves¹⁴, A. Aman¹⁵, H. Amar¹⁶, P. Amedo^{17,16}, J. Anderson¹⁸, D. A. Andrade¹⁹, C. Andreopoulos²⁰, M. Andreotti^{21,22}, M. P. Andrews³, F. Andrianala²³, S. Andringa²⁴, F. Anjarazafy²³, S. Ansarifard¹, D. Antic²⁵, M. Antoniaassi⁴, A. Aranda-Fernandez²⁶, L. Arellano²⁷, E. Arrieta Diaz²⁸, M. A. Arroyave³, M. Arteropons²⁹, J. Asadi³⁰, M. Ascencio³¹, A. Ashkenazi³², D. Asner³³, L. Asquith³⁴, E. Atkin¹⁴, D. Auguste³⁵, A. Aurisano³⁶, V. Aushev³⁷, D. Autiero³⁸, D. Ávila Gómez³⁹, M. B. Azam¹⁹, F. Azfar⁴⁰, A. Back⁴¹, J. J. Back⁴², Y. Bae⁴³, I. Bagaturia⁶, L. Bagby³, D. Baigarashev⁴⁴, S. Balasubramanian³, A. Balboni^{22,21}, P. Baldi⁴⁵, W. Baldini²¹, J. Baldonado⁴⁶, B. Baller³, B. Bambah⁴⁷, F. Barao^{24,48}, D. Barbu⁴⁹, G. Barenboim¹⁶, P. Barham Alzás², G. J. Barker⁴², W. Barkhouse⁵⁰, G. Barr⁴⁰, A. Barros⁴, N. Barros^{24,51}, D. Barrow⁴⁰, J. L. Barrow⁴³, A. Basharina-Freshville⁵², A. Bashyal³³, V. Basque³, M. Bassani⁵³, D. Basu⁵⁴, C. Batchelor⁵⁵, L. Bathe-Peters⁴⁰, J.B.R. Battat⁵⁶, F. Battisti⁵⁷, J. Bautista⁴³, F. Bay⁵⁸, J. L. L. Bazo Alba⁵⁹, J. F. Beacom⁶⁰, E. Bechettoille³⁸, B. Behera⁶¹, E. Belchior⁶², B. Bell⁶³, G. Bell⁶⁴, L. Bellantoni³, G. Bellettini^{65,66}, V. Bellini^{67,68}, O. Beltramello², A. Belyaev⁶⁹, C. Benitez Montiel^{16,70}, D. Benjamin³³, F. Bento Neves²⁴, J. Berger⁷¹, S. Berkman⁷², J. Bermudez⁷³, J. Bernal⁷⁰, P. Bernardini^{9,74}, A. Bersani⁷⁵, E. Bertholet³², E. Bertolini⁷⁶, S. Bertolucci^{57,77}, M. Betancourt³, A. Betancur Rodríguez³⁹, Y. Bezawada⁷⁸, A. T. Bezerra⁷⁹, A. Bhat⁸⁰, V. Bhatnagar⁸¹, M. Bhattacharjee⁸², S. Bhattacharjee⁶², M. Bhattacharya³, S. Bhuller⁴⁰, B. Bhuyan⁸², S. Biagi⁸³, J. Bian⁴⁵, K. Biery³, B. Bilki^{84,85}, M. Bishai³³, A. Blake⁸⁶, F. D. Blaszczyk³, G. C. Blazey⁵⁴, E. Blucher⁸⁰, B. Bogart⁸⁷, J. Boissevain⁸⁸, S. Bolognesi⁸⁹, T. Bolton¹¹, L. Bomben^{76,90}, M. Bonesini^{76,91}, C. Bonilla-Diaz⁹², A. Booth⁹³, F. Boran⁴¹, R. Borges Merlo⁷, N. Bostan⁸⁵, G. Botogoske⁹⁴, B. Bottino^{75,95}, R. Bouet⁹⁶, J. Boza⁷¹, J. Bracinik⁹⁷, B. Brahma⁹⁸, D. Brailsford⁸⁶, F. Bramati⁷⁶, A. Branca⁷⁶, A. Brandt³⁰, J. Bremer², S. J. Brice³, V. Brio⁶⁷, C. Brizzolari^{76,91}, C. Bromberg⁷², J. Brooke²⁵, A. Bross³, G. Brunetti^{76,91}, M. B. Brunetti⁹⁹, N. Buchanan⁷¹, H. Budd⁸, J. Buerger¹⁰⁰, A. Bundock²⁵, D. Burgardt¹⁰¹, S. Butchart³⁴, G. Caceres V.⁷⁸, R. Calabrese⁹⁴, R. Calabrese^{21,22}, J. Calcutt^{33,102}, L. Calivers¹⁰⁰, E. Calvo¹³, A. Caminata⁷⁵, A. F. Camino¹⁰³, W. Campanelli²⁴, A. Campani^{75,95}, A. Campos Benitez¹⁰⁴, N. Canci⁹⁴, J. Capó¹⁶, I. Caracas¹⁰⁵, D. Caratelli¹⁰⁶, D. Carber⁷¹, J. M. Carceller², G. Carini³³, B. Carlus³⁸, M. F. Carneiro³³, P. Carniti^{76,91}, I. Caro Terrazas⁷¹, H. Carranza³⁰, N. Carrara⁷⁸, L. Carroll¹¹, T. Carroll¹⁰⁷, A. Carter¹⁰⁸, E. Casarejos⁴⁶, D. Casazza²¹, J. F. Castaño Forero¹⁰⁹, F. A. Castaño¹¹⁰, C. Castromonte¹¹¹, E. Catano-Mur¹¹², C. Cattadori⁷⁶, F. Cavalier³⁵, F. Cavanna³, S. Centro²⁹, G. Cerati³, C. Cerna¹¹³, A. Cervelli⁵⁷, A. Cervera Villanueva¹⁶, J. Chakrani¹¹⁴, M. Chalifour², A. Chappell⁴², A. Chatterjee¹¹⁵, B. Chauhan⁸⁵, C. Chavez Barajas²⁰, H. Chen³³, M. Chen⁴⁵, W. C. Chen¹¹⁶, Y. Chen¹¹⁷, Z. Chen⁴⁵, D. Cherdack¹¹⁸, S. S. Chhibra⁹³, C. Chi¹¹⁹, F. Chiapponi⁵⁷, R. Chirco¹⁹, N. Chitirasreemadam^{65,66}, K. Cho¹²⁰, S. Choate⁸⁵, G. Choi⁸, D. Chokheli⁶, P. S. Chong¹²¹, B. Chowdhury¹⁸, D. Christian³, M. Chung¹²², E. Church¹²³, M. F. Cicala⁵², M. Cicerchia²⁹, V. Cicero^{57,77}, R. Ciolini⁶⁵, P. Clarke⁵⁵, G. Cline¹¹⁴, A. G. Cocco⁹⁴, J. A. B. Coelho¹²⁴, A. Cohen¹²⁴, J. Collazo⁴⁶, J. Collot¹²⁵, H. Combs¹⁰⁴, J. M. Conrad¹²⁶, L. Conti¹²⁷, T. Contreras³, M. Convery¹¹⁷, K. Conway¹²⁸, S. Copello¹²⁹, P. Cova^{53,130}, C. Cox¹⁰⁸, L. Cremonesi⁹³, J. I. Crespo-Anadón¹³, M. Crisler³, E. Cristaldo^{76,70}, J. Crnkovic³, G. Crone⁵², R. Cross⁴²,

Received:

Revised:

Accepted:

Published:

Citation: . Operation of a Modular 3D-Pixelated Liquid Argon Time-Projection Chamber in a Neutrino Beam. *Instruments* 2025, 1, 0. <https://doi.org/>

Copyright: © 2025 by the authors. Submitted to *Instruments* for possible open access publication under the terms and conditions of the Creative Commons Attribution (CC BY) license (<https://creativecommons.org/licenses/by/4.0/>).

A. Cudd¹⁰, C. Cuesta¹³, Y. Cui¹³¹, F. Curciarello¹³², D. Cussans²⁵, J. Dai¹²⁵, O. Dalager³,
 W. Dallaway¹¹⁶, R. D'Amico^{21,22}, H. da Motta¹³³, Z. A. Dar¹¹², R. Darby³⁴, L. Da
 Silva Peres¹³⁴, Q. David³⁸, G. S. Davies¹³⁵, S. Davini⁷⁵, J. Dawson¹²⁴, R. De Aguiar⁷,
 P. Debbins⁸⁵, M. P. Decowski^{136,137}, A. de Gouvêa¹³⁸, P. C. De Holanda⁷, P. De Jong^{136,137},
 P. Del Amo Sanchez¹³⁹, G. De Lauretis³⁸, A. Delbart⁸⁹, M. Delgado^{76,91}, A. Dell'Acqua²,
 G. Delle Monache¹³², N. Delmonte^{53,130}, P. De Lurgio¹⁸, R. Demario⁷², G. De Matteis^{9,74},
 J. R. T. de Mello Neto¹³⁴, A. P. A. De Mendonca⁷, D. M. DeMuth¹⁴⁰, S. Dennis¹⁴¹,
 C. Densham¹⁴², P. Denton³³, G. W. Deptuch³³, A. De Roeck², V. De Romeri¹⁶, J. P. Detje¹⁴¹,
 J. Devine², K. Dhanmeher³⁸, R. Dharmapalan¹⁴³, M. Dias¹⁴⁴, A. Diaz¹⁴⁵, J. S. Díaz⁴¹,
 F. Díaz⁵⁹, F. Di Capua^{94,146}, A. Di Domenico^{147,148}, S. Di Domizio^{75,95}, S. Di Falco⁶⁵,
 L. Di Giulio², P. Ding³, L. Di Noto^{75,95}, E. Diociaiuti¹³², G. Di Sciascio¹²⁷, V. Di
 Silvestre¹⁴⁷, C. Distefano⁸³, R. Di Stefano¹²⁷, R. Diurba¹⁰⁰, M. Diwan³³, Z. Djurcic¹⁸,
 S. Dolan², M. Dolce¹⁰¹, M. J. Dolinski⁶³, D. Domenici¹³², S. Dominguez¹³, S. Donati^{65,66},
 S. Doran³¹, D. Douglas¹¹⁷, T.A. Doyle¹²⁸, F. Drielsma¹¹⁷, D. Duchesneau¹³⁹, K. Duffy⁴⁰,
 K. Dugas⁴⁵, P. Dunne¹⁴, B. Dutta¹⁴⁹, D. A. Dwyer¹¹⁴, A. S. Dyshkant⁵⁴, S. Dytman¹⁰³,
 M. Eads⁵⁴, A. Earle³⁴, S. Edayath³¹, D. Edmunds⁷², J. Eisch³, W. Emark⁵⁴, P. Englezos¹⁵⁰,
 A. Ereditato⁸⁰, T. Erjavec⁷⁸, C. O. Escobar³, J. J. Evans²⁷, E. Ewart⁴¹, A. C. Ezeribe¹⁵¹,
 K. Fahey³, A. Falcone^{76,91}, M. Fani^{43,88}, D. Faragher⁴³, C. Farnese⁷³, Y. Farzan¹, J. Felix¹⁵²,
 Y. Feng³¹, M. Ferreira da Silva¹⁴⁴, G. Ferry³⁵, E. Fialova¹⁵³, L. Fields¹⁵⁴, P. Filip¹⁵⁵,
 A. Filkins¹⁵⁶, F. Filthaut^{136,157}, G. Fiorillo^{94,146}, M. Fiorini^{21,22}, S. Fogarty⁷¹, W. Foreman⁸⁸,
 J. Fowler¹⁵⁸, J. Franc¹⁵³, K. Francis⁵⁴, D. Franco⁸⁰, J. Franklin¹⁵⁹, J. Freeman³, J. Fried³³,
 A. Friedland¹¹⁷, M. Fucci¹²⁸, S. Fuess³, I. K. Furic¹⁶⁰, K. Furman⁹³, A. P. Furmanskii⁴³,
 R. Gaba⁸¹, A. Gabrielli^{57,77}, A. M. Gago⁵⁹, F. Galizzi^{76,91}, H. Gallagher¹⁶¹, M. Galli¹²⁴,
 N. Gallice³³, V. Galymov³⁸, E. Gamberini², T. Gamble¹⁵¹, R. Gandhi¹⁶², S. Ganguly³,
 F. Gao¹⁰⁶, S. Gao³³, D. Garcia-Gamez¹⁶³, M. Á. García-Peris²⁷, S. Gardiner³, A. Gartman¹⁵³,
 A. Gauch¹⁰⁰, P. Gauzzi^{147,148}, S. Gazzana¹³², G. Ge¹¹⁹, N. Geffroy¹³⁹, B. Gelli⁷, S. Gent¹⁶⁴,
 L. Gerlach³³, A. Ghosh³¹, T. Giammaria^{21,22}, D. Gibin^{29,73}, I. Gil-Botella¹³, A. Gioiosa¹²⁷,
 S. Giovannella¹³², A. K. Giri⁹⁸, V. Giusti⁶⁵, D. Gnani¹¹⁴, O. Gogota³⁷, S. Gollapinni⁸⁸,
 K. Gollwitzer³, R. A. Gomes¹⁶⁵, L. S. Gomez Fajardo¹⁶⁶, D. Gonzalez-Diaz¹⁷, J. Gonzalez-
 Santome², M. C. Goodman¹⁸, S. Goswami¹¹⁵, C. Gotti⁷⁶, J. Goudeau⁶², C. Grace¹¹⁴,
 E. Gramellini²⁷, R. Gran¹⁶⁷, P. Granger², C. Grant¹⁶⁸, D. R. Gratieri^{169,7}, G. Grauso⁹⁴,
 P. Green⁴⁰, S. Greenberg^{114,170}, W. C. Griffith³⁴, K. Grzelak¹⁷¹, L. Gu⁸⁶, W. Gu³³,
 V. Guarino¹⁸, M. Guarise^{21,22}, R. Guenette²⁷, M. Guerzoni⁵⁷, D. Guffanti^{76,91}, A. Guglielmi⁷³,
 F. Y. Guo¹²⁸, A. Gupta¹⁷², V. Gupta^{136,137}, G. Gurung³⁰, D. Gutierrez¹⁷³, P. Guzowski²⁷,
 M. M. Guzzo⁷, S. Gwon¹⁷⁴, A. Habig¹⁶⁷, L. Haegel³⁸, R. Hafeji^{16,17}, L. Hagaman⁸⁰,
 A. Hahn³, J. Hakenmüller¹⁵⁸, T. Hamernik³, P. Hamilton¹⁴, J. Hancock⁹⁷, M. Handley¹⁴¹,
 F. Happacher¹³², B. Harris¹²¹, D. A. Harris^{175,3}, L. Harris¹⁴³, A. L. Hart⁹³, J. Hartnell³⁴,
 T. Hartnett¹⁴², J. Harton⁷¹, T. Hasegawa¹⁷⁶, C. M. Hasnip², R. Hatcher³, S. Hawkins⁷²,
 J. Hays⁹³, M. He¹¹⁸, A. Heavey³, K. M. Heeger¹⁷⁷, A. Heindel¹²⁸, J. Heise¹⁷⁸, P. Hellmuth⁹⁶,
 L. Henderson¹⁰², K. Herner³, V. Hewes³⁶, A. Higuera¹⁷⁹, A. Himmel³, E. Hinkle⁸⁰,
 L.R. Hirsch⁴, J. Ho¹⁸⁰, J. Hoefken Zink⁵⁷, J. Hoff³, A. Holin¹⁴², T. Holvey⁴⁰, C. Hong¹²⁴,
 S. Horiuchi¹⁰⁴, G. A. Horton-Smith¹¹, R. Hosokawa¹⁸¹, T. Houdy³⁵, B. Howard^{175,3},
 R. Howell⁸, I. Hristova¹⁴², M. S. Hronek³, H. Hua¹⁴, J. Huang⁷⁸, R.G. Huang¹¹⁴,
 X. Huang¹³⁵, Z. Hulcher¹¹⁷, A. Hussain¹¹, G. Iles¹⁴, N. Ilic¹¹⁶, A. M. Iliescu¹³²,
 R. Illingworth³, G. Ingrassia¹⁷⁵, A. Ioannisian⁶⁹, M. Ismerio Oliveira¹³⁴, C.M. Jackson¹²³,
 V. Jain¹⁸², E. James³, W. Jang³⁰, B. Jargowsky⁴⁵, D. Jena³, I. Jentz¹⁰⁷, C. Jiang¹⁸³,
 J. Jiang¹²⁸, A. Jipa⁴⁹, J. H. Jo³³, F. R. Joaquim^{24,48}, W. Johnson⁶¹, C. Jollet⁹⁶, R. Jones¹⁵¹,
 N. Jovancevic¹⁸⁴, M. Judah¹⁰³, C. K. Jung¹²⁸, K. Y. Jung⁸, T. Junk³, Y. Jwa^{117,119},
 M. Kabirnezhad¹⁴, A. C. Kaboth^{108,142}, I. Kadenko³⁷, O. Kalikulov⁴⁴, D. Kalra¹¹⁹,
 M. Kandemir¹⁸⁵, S. Kar²⁵, G. Karagiorgi¹¹⁹, G. Karaman⁸⁵, A. Karcher¹¹⁴, Y. Karyotakis¹³⁹,

S. P. Kasetti⁶², L. Kashur⁷¹, A. Kauther⁵⁴, N. Kazaryan⁶⁹, L. Ke³³, E. Kearns¹⁶⁸, P.T. Keener¹²¹, K.J. Kelly¹⁴⁹, R. Keloth¹⁰⁴, E. Kemp⁷, O. Kemularia⁶, Y. Kermaidie³⁵, W. Ketchum³, S. H. Kettell³³, N. Khan¹⁴, A. Khvedelidze⁶, D. Kim¹⁴⁹, J. Kim⁸, M. J. Kim³, S. Kim¹⁷⁴, B. King³, M. King⁸⁰, M. Kirby³³, A. Kish³, J. Klein¹²¹, J. Kleykamp¹³⁵, A. Klustova¹⁴, T. Kobilarcik³, L. Koch¹⁰⁵, K. Koehler¹⁰⁷, L. W. Koerner¹¹⁸, D. H. Koh¹¹⁷, M. Kordosky¹¹², T. Kosci¹²⁵, V. A. Kostelecký⁴¹, I. Kotler⁶³, W. Krah¹³⁶, R. Kralik³⁴, M. Kramer¹¹⁴, F. Krennrich³¹, T. Kroupova¹²¹, S. Kubota²⁷, M. Kubu², V. A. Kudryavtsev¹⁵¹, G. Kufatty¹⁵, S. Kuhlmann¹⁸, A. Kumar⁴³, J. Kumar¹⁴³, M. Kumar¹⁷², P. Kumar¹⁸⁶, P. Kumar¹⁵¹, S. Kumaran⁴⁵, J. Kunzmann¹⁰⁰, V. Kus¹⁵³, T. Kutter⁶², J. Kvasnicka¹⁵⁵, T. Labree⁵⁴, M. Lachat⁸, T. Lackey³, I. Lalău⁴⁹, A. Lambert¹¹⁴, B. J. Land¹²¹, C. E. Lane⁶³, N. Lane²⁷, K. Lang¹⁸⁷, T. Langford¹⁷⁷, M. Langstaff²⁷, F. Lanni², J. Larkin⁸, P. Lasorak¹⁴, D. Last⁸, A. Laudrie¹⁰⁷, G. Laurenti⁵⁷, E. Lavaut³⁵, H. Lay⁸⁶, I. Lazanu⁴⁹, R. LaZur⁷¹, M. Lazzaroni^{53,188}, S. Leardini¹⁷, J. Learned¹⁴³, T. LeCompte¹¹⁷, G. Lehmann Miotto², R. Lehnert⁴¹, M. Leitner¹¹⁴, H. Lemoine¹⁶⁷, D. Leon Silverio⁶¹, L. M. Lepin¹⁵, J.-Y. Li⁵⁵, S. W. Li⁴⁵, Y. Li³³, R. Lima⁷⁹, C. S. Lin¹¹⁴, D. Lindebaum²⁵, S. Linden³³, R. A. Lineros⁹², A. Lister¹⁰⁷, B. R. Littlejohn¹⁹, J. Liu⁴⁵, Y. Liu⁸⁰, S. Lockwitz³, I. Lomidze⁶, K. Long¹⁴, J. Lopez¹¹⁰, I. López de Rego¹³, N. López-March¹⁶, J. M. LoSecco¹⁵⁴, A. Lozano Sanchez⁶³, X.-G. Lu⁴², K.B. Luk^{189,114,170}, X. Luo¹⁰⁶, E. Luppi^{21,22}, A. A. Machado⁷, P. Machado³, C. T. Macias⁴¹, J. R. Macier³, M. MacMahon⁵², S. Magill¹⁸, C. Magueur³⁵, K. Mahn⁷², A. Maio^{24,51}, N. Majeed¹¹, A. Major¹⁵⁸, K. Majumdar²⁰, A. Malige¹¹⁹, S. Mamelj⁶⁵, M. Man¹¹⁶, R. C. Mandujano⁴⁵, J. Maneira^{24,51}, S. Manly⁸, K. Manolopoulos¹⁴², M. Manrique Plata⁴¹, S. Manthey Corchado¹³, L. Manzanillas-Velez¹³⁹, E. Mao¹⁵⁶, M. Marchan³, A. Marchionni³, D. Marfatia¹⁴³, C. Mariani¹⁰⁴, J. Maricic¹⁴³, F. Marinho¹⁹⁰, A. D. Marino¹⁰, T. Markiewicz¹¹⁷, F. Das Chagas Marques⁷, M. Marshak⁴³, C. M. Marshall⁸, J. Marshall⁴², L. Martina^{9,74}, J. Martín-Albo¹⁶, D.A. Martinez Caicedo⁶¹, M. Martinez-Casales³, F. Martínez López⁴¹, S. Martynenko³³, V. Mascagna⁷⁶, A. Mastbaum¹⁵⁰, M. Masud¹⁷⁴, F. Matichard¹¹⁴, G. Matteucci^{94,146}, J. Matthews⁶², C. Mauger¹²¹, N. Mauri^{57,77}, K. Mavrokoridis²⁰, I. Mawby⁸⁶, F. Mayhew⁷², T. McAskill⁵⁶, N. McConkey⁹³, B. McConnell⁴¹, K. S. McFarland⁸, C. McGivern³, C. McGrew¹²⁸, A. McNab²⁷, C. McNulty¹¹⁴, J. Mead¹³⁶, L. Meazza⁷⁶, V. C. N. Meddage¹⁶⁰, A. Medhi⁸², M. Mehmood¹⁷⁵, B. Mehta⁸¹, P. Mehta¹⁸⁶, F. Mei^{57,77}, P. Melas¹⁹¹, L. Mellet⁷², T. C. D. Melo⁷⁹, O. Mena¹⁶, H. Mendez¹⁷³, D. P. Méndez³³, A. Menegolli^{129,192}, G. Meng⁷³, A. C. E. A. Mercuri⁴, A. Meregaglia⁹⁶, M. D. Messier⁴¹, S. Metallo⁴³, W. Metcalf⁶², M. Mewes⁴¹, H. Meyer¹⁰¹, T. Miao³, J. Micallef^{161,126}, A. Miccoli⁹, G. Michna¹⁶⁴, R. Milincic¹⁴³, F. Miller¹⁰⁷, G. Miller²⁷, W. Miller⁴³, A. Minotti^{76,91}, L. Miralles Verge², C. Mironov¹²⁴, S. Miscetti¹³², C. S. Mishra³, P. Mishra⁴⁷, S. R. Mishra¹⁹³, D. Mladenov², I. Mocioiu¹⁹⁴, A. Mogan³, R. Mohanta⁴⁷, T. A. Mohayai⁴¹, N. Mokhov³, J. Molina⁷⁰, L. Molina Bueno¹⁶, E. Montagna^{57,77}, A. Montanari⁵⁷, C. Montanari^{129,3,192}, D. Montanari³, D. Montanino^{9,74}, L. M. Montaña Zetina¹⁹⁵, M. Mooney⁷¹, A. F. Moor¹⁵¹, M. Moore¹¹⁷, Z. Moore¹⁵⁶, D. Moreno¹⁰⁹, G. Moreno-Granados¹⁰⁴, O. Moreno-Palacios¹¹², L. Morescalchi⁶⁵, C. Morris¹¹⁸, E. Motuk⁵², C. A. Moura¹⁹⁶, G. Moustier⁸⁶, W. Mu³, L. Muallem¹⁴⁵, J. Mueller³, M. Muether¹⁰¹, A. Muir⁶⁴, Y. Mukhamejanov⁴⁴, A. Mukhamejanova⁴⁴, M. Mulhearn⁷⁸, D. Munford¹¹⁸, L. J. Munteanu², H. Muramatsu⁴³, J. Muraz¹²⁵, M. Murphy¹⁰⁴, T. Murphy¹⁵⁶, A. Mytilinaki¹⁴², J. Nachtman⁸⁵, Y. Nagai¹⁹⁷, S. Nagu¹⁹⁸, D. Naples¹⁰³, S. Narita¹⁸¹, J. Nava^{57,77}, A. Navrer-Agasson^{14,27}, N. Nayak³³, M. Nebot-Guinot⁵⁵, A. Nehm¹⁰⁵, J. K. Nelson¹¹², O. Neogi⁸⁵, J. Nesbit¹⁰⁷, M. Nessi^{3,2}, D. Newbold¹⁴², M. Newcomer¹²¹, D. Newmark¹²⁶, R. Nichol⁵², F. Nicolas-Arnaldos¹⁶³, A. Nielsen⁴⁵, A. Nikolica¹²¹, J. Nikolov¹⁸⁴, E. Niner³, X. Ning³³, K. Nishimura¹⁴³, A. Norman³, A. Norrick³, P. Novella¹⁶, A. Nowak⁸⁶, J. A. Nowak⁸⁶, M. Oberling¹⁸, J. P. Ochoa-Ricoux⁴⁵, S. Oh¹⁵⁸, S.B. Oh³, A. Olivier¹⁵⁴, T. Olson¹¹⁸, Y. Onel⁸⁵, Y. Onishchuk³⁷, A. Oranday⁴¹, M. Osbiston⁴², J. A. Osorio Vélez¹¹⁰,

L. O'Sullivan¹⁰⁵, L. Otiniano Ormachea^{199,111}, L. Pagani⁷⁸, G. Palacio³⁹, O. Palamara³, S. Palestini²⁰⁰, J. M. Paley³, M. Pallavicini^{75,95}, C. Palomares¹³, S. Pan¹¹⁵, M. Panareo^{9,74}, P. Panda⁴⁷, V. Pandey³, W. Panduro Vazquez¹⁰⁸, E. Pantic⁷⁸, V. Paolone¹⁰³, A. Papadopoulou⁸⁸, R. Papaleo⁸³, D. Papoulias¹⁹¹, S. Paramesvaran²⁵, J. Park¹⁷⁴, S. Parke³, S. Parsa¹⁰⁰, S. Parveen¹⁸⁶, M. Parvu⁴⁹, D. Pasciuto⁶⁵, S. Pascoli^{57,77}, L. Pasqualini^{57,77}, J. Pasternak¹⁴, G. Patel⁴³, J. L. Paton³, C. Patrick⁵⁵, L. Patrizii⁵⁷, R. B. Patterson¹⁴⁵, T. Patzak¹²⁴, A. Paudel³, J. Paul¹³⁶, L. Paulucci¹⁹⁰, Z. Pavlovic³, G. Pawloski⁴³, D. Payne²⁰, A. Peake¹⁰⁸, V. Pec¹⁵⁵, E. Pedreschi⁶⁵, S. J. M. Peeters³⁴, W. Pellico³, E. Pennacchio³⁸, A. Penzo⁸⁵, O. L. G. Peres⁷, Y. F. Perez Gonzalez¹⁵⁹, L. Pérez-Molina¹³, C. Pernas¹¹², J. Perry⁵⁵, D. Pershey¹⁵, G. Pessina⁷⁶, G. Petrillo¹¹⁷, C. Petta^{67,68}, R. Petti¹⁹³, M. Pfaff¹⁴, V. Pia^{57,77}, G. M. Piacentino¹²⁷, L. Pickering^{142,108}, L. Pierini^{22,21}, F. Pietropaolo^{2,73}, V.L.Pimentel^{201,7}, G. Pinaroli³³, S. Pincha⁸², J. Pinchault¹³⁹, K. Pitts¹⁰⁴, P. Plesniak¹⁴, K. Pletcher⁷², K. Plows⁴⁰, C. Pollack¹⁷³, T. Pollmann^{136,137}, F. Pompa¹⁶, X. Pons², N. Poonthottathil^{172,31}, V. Popov³², F. Poppi^{57,77}, J. Porter³⁴, L. G. Porto Paixão⁷, M. Potekhin³³, M. Pozzato^{57,77}, R. Pradhan⁹⁸, T. Prakash¹¹⁴, M. Prest⁷⁶, F. Psihas³, D. Pugnere³⁸, D. Pullia^{2,124}, X. Qian³³, J. Queen¹⁵⁸, J. L. Raaf³, M. Rabelhofer⁴¹, V. Radeka³³, J. Rademacker²⁵, F. Raffaelli⁶⁵, A. Rafique¹⁸, A. Rahe⁵⁴, S. Rajagopalan³³, M. Rajaoalisoa³⁶, I. Rakhno³, L. Rakotondravohitra²³, M. A. Ralaikoto²³, L. Ralte⁹⁸, M. A. Ramirez Delgado¹²¹, B. Ramson³, S. S. Randriamanampisoa²³, A. Rappoldi^{129,192}, G. Raselli^{129,192}, T. Rath⁶¹, P. Ratoff⁸⁶, R. Ray³, H. Razafinime³⁶, R. F. Razakamiandra¹²⁸, E. M. Rea⁴³, J. S. Real¹²⁵, B. Rebel^{107,3}, R. Rechenmacher³, J. Reichenbacher⁶¹, S. D. Reitzner³, E. Renner⁸⁸, S. Repetto^{75,95}, S. Rescia³³, F. Resnati², C. Reynolds⁹³, M. Ribas⁴, S. Riboldi⁵³, C. Riccio¹²⁸, G. Riccobene⁸³, J. S. Ricol¹²⁵, M. Rigan³⁴, A. Rikalo¹⁸⁴, E. V. Rincón³⁹, A. Ritchie-Yates¹⁰⁸, D. Rivera⁸⁸, A. Robert¹²⁵, A. Roberts²⁰, E. Robles⁴⁵, M. Roda²⁰, D. Rodas Rodríguez¹⁷, M. J. O. Rodrigues⁷⁹, J. Rodriguez Rondon⁶¹, S. Rosauro-Alcaraz³⁵, P. Rosier³⁵, D. Ross⁷², M. Rossella^{129,192}, M. Ross-Lonergan¹¹⁹, T. Rotsy²³, N. Roy¹⁷⁵, P. Roy¹⁰¹, P. Roy¹⁰⁴, C. Rubbia²⁰², D. Rudik⁹⁴, A. Ruggeri⁵⁷, G. Ruiz Ferreira²⁷, K. Rushiya¹⁸⁶, B. Russell¹²⁶, S. Sacerdoti¹²⁴, N. Saduyev⁴⁴, S. K. Sahoo⁹⁸, N. Sahu⁹⁸, S. Sakhiyev⁴⁴, P. Sala³, G. Salmoria⁴, S. Samanta⁷⁵, M. C. Sanchez¹⁵, A. Sánchez-Castillo¹⁶³, P. Sanchez-Lucas¹⁶³, D. A. Sanders¹³⁵, S. Sanfilippo⁸³, D. Santoro^{53,130}, N. Saoulidou¹⁹¹, P. Sapienza⁸³, I. Sarcevic²⁰³, I. Sarra¹³², G. Savage³, V. Savinov¹⁰³, G. Scanavini¹⁷⁷, A. Scanu⁷⁶, A. Scaramelli¹²⁹, T. Schefke⁶², H. Schellman^{102,3}, S. Schifano^{21,22}, P. Schlabach³, D. Schmitz⁸⁰, A. W. Schneider¹²⁶, K. Scholberg¹⁵⁸, A. Schroeder⁴³, A. Schukraft³, B. Schuld¹⁰, S. Schwartz¹⁴⁵, A. Segade⁴⁶, E. Segreto⁷, A. Selyunin¹⁰⁰, C. R. Senise¹⁴⁴, J. Sensenig¹²¹, S.H. Seo³, D. Seppela⁷², M. H. Shaevitz¹¹⁹, P. Shanahan³, P. Sharma⁸¹, R. Kumar²⁰⁴, S. Sharma Poudel⁶¹, K. Shaw³⁴, T. Shaw³, K. Shchablo³⁸, J. Shen¹²¹, C. Shepherd-Themistocleous¹⁴², J. Shi¹⁴¹, W. Shi¹²⁸, S. Shin²⁰⁵, S. Shivakoti¹⁰¹, A. Shmakov⁴⁵, I. Shoemaker¹⁰⁴, D. Shooltz⁷², R. Shrock¹²⁸, M. Siden⁷¹, J. Silber¹¹⁴, L. Simard³⁵, J. Sinclair¹¹⁷, G. Sinev⁶¹, Jaydip Singh⁷⁸, J. Singh¹⁹⁸, L. Singh²⁰⁶, P. Singh⁹³, V. Singh²⁰⁶, S. Singh Chauhan⁸¹, R. Sipos², C. Sironneau¹²⁴, G. Sirri⁵⁷, K. Siyeon¹⁷⁴, K. Skarpaas¹¹⁷, J. Smedley⁸, J. Smith¹²⁸, P. Smith⁴¹, J. Smolik^{153,155}, M. Smy⁴⁵, M. Snape⁴², E.L. Snider³, P. Snopok¹⁹, M. Soares Nunes³, H. Sobel⁴⁵, M. Soderberg¹⁵⁶, H. Sogarwal³¹, C. J. Solano Salinas²⁰⁷, S. Söldner-Rembold¹⁴, N. Solomey¹⁰¹, V. Solovov²⁴, W. E. Sondheim⁸⁸, M. Sorbara¹²⁷, M. Sorel¹⁶, J. Soto-Oton¹⁶, A. Sousa³⁶, K. Soustruznik²⁰⁸, D. Souza Correia¹³³, F. Spinella⁶⁵, J. Spitz⁸⁷, N. J. C. Spooner¹⁵¹, D. Stalder⁷⁰, M. Stancari³, L. Stanco^{29,73}, J. Steenis⁷⁸, R. Stein²⁵, H. M. Steiner¹¹⁴, A. F. Steklain Lisboa⁴, J. Stewart³³, B. Stillwell⁸⁰, J. Stock⁶¹, T. Stokes¹⁷⁷, T. Strauss³, L. Strigari¹⁴⁹, A. Stuart²⁶, J. G. Suarez³⁹, J. Subash⁹⁷, A. Surdo⁹, L. Suter³, A. Sutton¹⁵, K. Sutton¹⁴⁵, Y. Suvorov^{94,146}, R. Svoboda⁷⁸, S. K. Swain²⁰⁹, C. Sweeney³¹, B. Szczerbinska²¹⁰, A. M. Szcl⁵⁵, A. Sztuc⁵², A. Taffara⁶⁵, N. Talukdar¹⁹³, J. Tamara¹⁰⁹, H. A. Tanaka¹¹⁷, S. Tang³³, N. Taniuchi¹⁴¹, A. M. Tapia

Casanova²¹¹, A. Tapper¹⁴, S. Tariq³, E. Tatar²¹², R. Tayloe⁴¹, A. M. Teklu¹²⁸, K. Tellez Giron Flores³³, J. Tena Vidal³², P. Tennesen^{114,58}, M. Tenti⁵⁷, K. Terao¹¹⁷, F. Terranova^{76,91}, G. Testera⁷⁵, T. Thakore³⁶, A. Thea¹⁴², S. Thomas¹⁵⁶, A. Thompson¹³⁸, C. Thorpe²⁷, S. C. Timm³, E. Tiras^{185,85}, V. Tishchenko³³, S. Tiwari⁸, N. Todorović¹⁸⁴, L. Tomassetti^{21,22}, A. Tonazzo¹²⁴, D. Torbunov³³, D. Torres Muñoz⁶¹, M. Torti^{76,91}, M. Tortola¹⁶, Y. Torun¹⁹, N. Tosi⁵⁷, D. Totani⁷¹, M. Touns³, C. Touramanis²⁰, V. Trabattoni⁵³, D. Tran¹¹⁸, J. Trevor¹⁴⁵, E. Triller⁷², S. Trilov²⁵, D. Trotta⁷⁶, J. Truchon¹⁰⁷, D. Truncali^{147,148}, W. H. Trzaska²¹³, Y. Tsai⁴⁵, Y.-T. Tsai¹¹⁷, Z. Tsamalaidze⁶, K. V. Tsang¹¹⁷, N. Tsverava⁶, S. Z. Tu¹⁸³, S. Tufanli², C. Tunnell¹⁷⁹, J. Turner¹⁵⁹, M. Tuzi¹⁶, M. Tzanov⁶², M. A. Uchida¹⁴¹, J. Ureña González¹⁶, J. Urheim⁴¹, T. Usher¹¹⁷, H. Utaegbulam⁸, S. Uzunyan⁵⁴, M. R. Vagins^{214,45}, P. Vahle¹¹², G. A. Valdivieso⁷⁹, E. Valencia¹⁵², R. Valentim¹⁴⁴, Z. Vallari⁶⁰, E. Vallazza⁷⁶, J. W. F. Valle¹⁶, R. Van Berg¹²¹, D. V. Forero²¹¹, A. Vannozzi¹³², M. Van Nuland-Troost¹³⁶, F. Varanini⁷³, D. Vargas Oliva¹¹⁶, N. Vaughan¹⁰², K. Vaziri³, A. Vázquez-Ramos¹⁶³, J. Vega¹⁹⁹, J. Vences^{24,51}, S. Ventura⁷³, A. Verdugo¹³, M. Verzocchi³, K. Vetter³, M. Vicenzi³³, H. Vieira de Souza¹²⁴, C. Vignoli²¹⁵, C. Vilela²⁴, E. Villa², S. Viola⁸³, B. Viren³³, G. V. Stenico⁵⁵, R. Vizarreta⁸, A. P. Vizcaya Hernandez⁷¹, S. Vlachos²⁷, G. Vorobyev¹⁹³, Q. Vuong⁸, A. V. Waldron⁹³, L. Walker¹¹⁸, H. Wallace¹⁰⁸, M. Wallach⁷², J. Walsh⁷², T. Walton³, L. Wan³, B. Wang⁸⁵, H. Wang²¹⁶, J. Wang⁶¹, M.H.L.S. Wang³, X. Wang³, Y. Wang²¹⁷, D. Warner⁷¹, L. Warsame¹⁴², M.O. Wascko^{40,142}, D. Waters⁵², A. Watson⁹⁷, K. Wawrowska^{142,34}, A. Weber^{105,3}, C. M. Weber⁴³, M. Weber¹⁰⁰, H. Wei⁶², A. Weinstein³¹, S. Westerdale¹³¹, M. Wetstein³¹, K. Whalen¹⁴², A.J. White⁸⁰, L. H. Whitehead¹⁴¹, D. Whittington¹⁵⁶, F. Wieler⁴, J. Wilhlemi¹⁷⁷, M. J. Wilking⁴³, A. Wilkinson⁴², C. Wilkinson¹¹⁴, F. Wilson¹⁴², R. J. Wilson⁷¹, P. Winter¹⁸, J. Wolcott¹⁶¹, J. Wolfs⁸, T. Wongjirad¹⁶¹, A. Wood¹¹⁸, K. Wood¹¹⁴, E. Worcester³³, M. Worcester³³, K. Wresilo¹⁴¹, M. Wright²⁷, M. Wrobel⁷¹, S. Wu⁴³, W. Wu⁴⁵, Z. Wu⁴⁵, M. Wurm¹⁰⁵, J. Wyenberg¹⁸⁰, B. M. Wynne⁵⁵, Y. Xiao⁴⁵, I. Xiotidis¹⁴, B. Yaeggy³⁶, N. Yahlali¹⁶, E. Yandel¹⁰⁶, G. Yang^{33,128}, J. Yang¹⁸⁹, T. Yang³, A. Yankelevich⁴⁵, L. Yates³, U. (. Yevarouskaya¹²⁸, K. Yonehara³, T. Young⁵⁰, B. Yu³³, H. Yu³³, J. Yu³⁰, W. Yuan⁵⁵, M. Zabloudil¹⁵³, R. Zaki¹⁷⁵, J. Zalesak¹⁵⁵, L. Zambelli¹³⁹, B. Zamorano¹⁶³, A. Zani⁵³, O. Zapata¹¹⁰, L. Zazueta¹⁵⁶, G. P. Zeller³, J. Zennamo³, J. Zettlemoyer³, K. Zeug¹⁰⁷, C. Zhang³³, S. Zhang⁴¹, Y. Zhang³³, L. Zhao⁴⁵, M. Zhao³³, E. D. Zimmerman¹⁰, S. Zucchelli^{57,77}, V. Zutshi⁵⁴, R. Zwaska³, and On behalf of the DUNE Collaboration

¹ Institute for Research in Fundamental Sciences, Tehran, Iran

² CERN, The European Organization for Nuclear Research, 1211 Meyrin, Switzerland

³ Fermi National Accelerator Laboratory, Batavia, IL 60510, USA

⁴ Universidade Tecnológica Federal do Paraná, Curitiba, Brazil

⁵ Universidad del Atlántico, Barranquilla, Atlántico, Colombia

⁶ Georgian Technical University, Tbilisi, Georgia

⁷ Universidade Estadual de Campinas, Campinas - SP, 13083-970, Brazil

⁸ University of Rochester, Rochester, NY 14627, USA

⁹ Istituto Nazionale di Fisica Nucleare Sezione di Lecce, 73100 - Lecce, Italy

¹⁰ University of Colorado Boulder, Boulder, CO 80309, USA

¹¹ Kansas State University, Manhattan, KS 66506, USA

¹² Augustana University, Sioux Falls, SD 57197, USA

¹³ CIEMAT, Centro de Investigaciones Energéticas, Medioambientales y Tecnológicas, E-28040 Madrid, Spain

¹⁴ Imperial College of Science, Technology and Medicine, London SW7 2BZ, United Kingdom

¹⁵ Florida State University, Tallahassee, FL, 32306 USA

¹⁶ Instituto de Física Corpuscular, CSIC and Universitat de València, 46980 Paterna, Valencia, Spain

¹⁷ Instituto Galego de Física de Altas Enerxías, University of Santiago de Compostela, Santiago de Compostela, 15782, Spain

¹⁸ Argonne National Laboratory, Argonne, IL 60439, USA

¹⁹ Illinois Institute of Technology, Chicago, IL 60616, USA

²⁰ University of Liverpool, L69 7ZE, Liverpool, United Kingdom

²¹ Istituto Nazionale di Fisica Nucleare Sezione di Ferrara, I-44122 Ferrara, Italy

- 22 University of Ferrara, Ferrara, Italy
23 University of Antananarivo, Antananarivo 101, Madagascar
24 Laboratório de Instrumentação e Física Experimental de Partículas, 1649-003 Lisboa and 3004-516 Coimbra, Portugal
25 University of Bristol, Bristol BS8 1TL, United Kingdom
26 Universidad de Colima, Colima, Mexico
27 University of Manchester, Manchester M13 9PL, United Kingdom
28 Universidad del Magdalena, Santa Marta - Colombia
29 Università degli Studi di Padova, I-35131 Padova, Italy
30 University of Texas at Arlington, Arlington, TX 76019, USA
31 Iowa State University, Ames, Iowa 50011, USA
32 Tel Aviv University, Tel Aviv-Yafo, Israel
33 Brookhaven National Laboratory, Upton, NY 11973, USA
34 University of Sussex, Brighton, BN1 9RH, United Kingdom
35 Université Paris-Saclay, CNRS/IN2P3, IJCLab, 91405 Orsay, France
36 University of Cincinnati, Cincinnati, OH 45221, USA
37 Taras Shevchenko National University of Kyiv, 01601 Kyiv, Ukraine
38 Institut de Physique des 2 Infinis de Lyon, 69622 Villeurbanne, France
39 Universidad EIA, Envigado, Antioquia, Colombia
40 University of Oxford, Oxford, OX1 3RH, United Kingdom
41 Indiana University, Bloomington, IN 47405, USA
42 University of Warwick, Coventry CV4 7AL, United Kingdom
43 University of Minnesota Twin Cities, Minneapolis, MN 55455, USA
44 Institute of Nuclear Physics at Almaty, Almaty 050032, Kazakhstan
45 University of California Irvine, Irvine, CA 92697, USA
46 University of Vigo, E- 36310 Vigo Spain
47 University of Hyderabad, Gachibowli, Hyderabad - 500 046, India
48 Instituto Superior Técnico - IST, Universidade de Lisboa, 1049-001 Lisboa, Portugal
49 University of Bucharest, Bucharest, Romania
50 University of North Dakota, Grand Forks, ND 58202-8357, USA
51 Faculdade de Ciências da Universidade de Lisboa - FCUL, 1749-016 Lisboa, Portugal
52 University College London, London, WC1E 6BT, United Kingdom
53 Istituto Nazionale di Fisica Nucleare Sezione di Milano, 20133 Milano, Italy
54 Northern Illinois University, DeKalb, IL 60115, USA
55 University of Edinburgh, Edinburgh EH8 9YL, United Kingdom
56 Wellesley College, Wellesley, MA 02481, USA
57 Istituto Nazionale di Fisica Nucleare Sezione di Bologna, 40127 Bologna BO, Italy
58 Antalya Bilim University, 07190 Döşemealtı/Antalya, Turkey
59 Pontificia Universidad Católica del Perú, Lima, Perú
60 Ohio State University, Columbus, OH 43210, USA
61 South Dakota School of Mines and Technology, Rapid City, SD 57701, USA
62 Louisiana State University, Baton Rouge, LA 70803, USA
63 Drexel University, Philadelphia, PA 19104, USA
64 Daresbury Laboratory, Cheshire WA4 4AD, United Kingdom
65 Istituto Nazionale di Fisica Nucleare Laboratori Nazionali di Pisa, Pisa PI, Italy
66 Università di Pisa, I-56127 Pisa, Italy
67 Istituto Nazionale di Fisica Nucleare Sezione di Catania, I-95123 Catania, Italy
68 Università di Catania, 2 - 95131 Catania, Italy
69 Yerevan Institute for Theoretical Physics and Modeling, Yerevan 0036, Armenia
70 Universidad Nacional de Asunción, San Lorenzo, Paraguay
71 Colorado State University, Fort Collins, CO 80523, USA
72 Michigan State University, East Lansing, MI 48824, USA
73 Istituto Nazionale di Fisica Nucleare Sezione di Padova, 35131 Padova, Italy
74 Università del Salento, 73100 Lecce, Italy
75 Istituto Nazionale di Fisica Nucleare Sezione di Genova, 16146 Genova GE, Italy
76 Istituto Nazionale di Fisica Nucleare Sezione di Milano Bicocca, 3 - I-20126 Milano, Italy
77 Università di Bologna, 40127 Bologna, Italy
78 University of California Davis, Davis, CA 95616, USA
79 Universidade Federal de Alfenas, Poços de Caldas - MG, 37715-400, Brazil
80 University of Chicago, Chicago, IL 60637, USA
81 Panjab University, Chandigarh, 160014, India
82 Indian Institute of Technology Guwahati, Guwahati, 781 039, India
83 Istituto Nazionale di Fisica Nucleare Laboratori Nazionali del Sud, 95123 Catania, Italy
84 Beykent University, Istanbul, Turkey
85 University of Iowa, Iowa City, IA 52242, USA

- 86 Lancaster University, Lancaster LA1 4YB, United Kingdom
- 87 University of Michigan, Ann Arbor, MI 48109, USA
- 88 Los Alamos National Laboratory, Los Alamos, NM 87545, USA
- 89 IRFU, CEA, Université Paris-Saclay, F-91191 Gif-sur-Yvette, France
- 90 University of Insubria, Via Ravasi, 2, 21100 Varese VA, Italy
- 91 Università di Milano Bicocca , 20126 Milano, Italy
- 92 Universidad Católica del Norte, Antofagasta, Chile
- 93 Queen Mary University of London, London E1 4NS, United Kingdom
- 94 Istituto Nazionale di Fisica Nucleare Sezione di Napoli, I-80126 Napoli, Italy
- 95 Università degli Studi di Genova, Genova, Italy
- 96 Laboratoire de Physique des Deux Infinis Bordeaux - IN2P3, F-33175 Gradignan, Bordeaux, France,
- 97 University of Birmingham, Birmingham B15 2TT, United Kingdom
- 98 Indian Institute of Technology Hyderabad, Hyderabad, 502285, India
- 99 University of Kansas, Lawrence, KS 66045
- 100 University of Bern, CH-3012 Bern, Switzerland
- 101 Wichita State University, Wichita, KS 67260, USA
- 102 Oregon State University, Corvallis, OR 97331, USA
- 103 University of Pittsburgh, Pittsburgh, PA 15260, USA
- 104 Virginia Tech, Blacksburg, VA 24060, USA
- 105 Johannes Gutenberg-Universität Mainz, 55122 Mainz, Germany
- 106 University of California Santa Barbara, Santa Barbara, CA 93106, USA
- 107 University of Wisconsin Madison, Madison, WI 53706, USA
- 108 Royal Holloway College London, London, TW20 0EX, United Kingdom
- 109 Universidad Antonio Nariño, Bogotá, Colombia
- 110 University of Antioquia, Medellín, Colombia
- 111 Universidad Nacional de Ingeniería, Lima 25, Perú
- 112 William and Mary, Williamsburg, VA 23187, USA
- 113 Particle Physics and Cosmology International Research Laboratory , Chicago IL, 60637 USA
- 114 Lawrence Berkeley National Laboratory, Berkeley, CA 94720, USA
- 115 Physical Research Laboratory, Ahmedabad 380 009, India
- 116 University of Toronto, Toronto, Ontario M5S 1A1, Canada
- 117 SLAC National Accelerator Laboratory, Menlo Park, CA 94025, USA
- 118 University of Houston, Houston, TX 77204, USA
- 119 Columbia University, New York, NY 10027, USA
- 120 Korea Institute of Science and Technology Information, Daejeon, 34141, South Korea
- 121 University of Pennsylvania, Philadelphia, PA 19104, USA
- 122 Ulsan National Institute of Science and Technology, Ulsan 689-798, South Korea
- 123 Pacific Northwest National Laboratory, Richland, WA 99352, USA
- 124 Université Paris Cité, CNRS, Astroparticule et Cosmologie, Paris, France
- 125 University Grenoble Alpes, CNRS, Grenoble INP, LPSC-IN2P3, 38000 Grenoble, France
- 126 Massachusetts Institute of Technology, Cambridge, MA 02139, USA
- 127 Istituto Nazionale di Fisica Nucleare Roma Tor Vergata , 00133 Roma RM, Italy
- 128 Stony Brook University, SUNY, Stony Brook, NY 11794, USA
- 129 Istituto Nazionale di Fisica Nucleare Sezione di Pavia, I-27100 Pavia, Italy
- 130 University of Parma, 43121 Parma PR, Italy
- 131 University of California Riverside, Riverside CA 92521, USA
- 132 Istituto Nazionale di Fisica Nucleare Laboratori Nazionali di Frascati, Frascati, Roma, Italy
- 133 Centro Brasileiro de Pesquisas Físicas, Rio de Janeiro, RJ 22290-180, Brazil
- 134 Universidade Federal do Rio de Janeiro, Rio de Janeiro - RJ, 21941-901, Brazil
- 135 University of Mississippi, University, MS 38677 USA
- 136 Nikhef National Institute of Subatomic Physics, 1098 XG Amsterdam, Netherlands
- 137 University of Amsterdam, NL-1098 XG Amsterdam, The Netherlands
- 138 Northwestern University, Evanston, IL 60208, USA
- 139 Laboratoire d'Annecy de Physique des Particules, Université Savoie Mont Blanc, CNRS, LAPP-IN2P3, 74000 Annecy, France
- 140 Valley City State University, Valley City, ND 58072, USA
- 141 University of Cambridge, Cambridge CB3 0HE, United Kingdom
- 142 STFC Rutherford Appleton Laboratory, Didcot OX11 0QX, United Kingdom
- 143 University of Hawaii, Honolulu, HI 96822, USA
- 144 Universidade Federal de São Paulo, 09913-030, São Paulo, Brazil
- 145 California Institute of Technology, Pasadena, CA 91125, USA
- 146 Università degli Studi di Napoli Federico II , 80138 Napoli NA, Italy
- 147 Sapienza University of Rome, 00185 Roma RM, Italy
- 148 Istituto Nazionale di Fisica Nucleare Sezione di Roma, 00185 Roma RM, Italy
- 149 Texas A&M University, College Station, Texas 77840

- 150 Rutgers University, Piscataway, NJ, 08854, USA
- 151 University of Sheffield, Sheffield S3 7RH, United Kingdom
- 152 Universidad de Guanajuato, Guanajuato, C.P. 37000, Mexico
- 153 Czech Technical University, 115 19 Prague 1, Czech Republic
- 154 University of Notre Dame, Notre Dame, IN 46556, USA
- 155 Institute of Physics, Czech Academy of Sciences, 182 00 Prague 8, Czech Republic
- 156 Syracuse University, Syracuse, NY 13244, USA
- 157 Radboud University, NL-6525 AJ Nijmegen, Netherlands
- 158 Duke University, Durham, NC 27708, USA
- 159 Durham University, Durham DH1 3LE, United Kingdom
- 160 University of Florida, Gainesville, FL 32611-8440, USA
- 161 Tufts University, Medford, MA 02155, USA
- 162 Harish-Chandra Research Institute, Jhansi, Allahabad 211 019, India
- 163 University of Granada & CAFPE, 18002 Granada, Spain
- 164 South Dakota State University, Brookings, SD 57007, USA
- 165 Universidade Federal de Goias, Goiania, GO 74690-900, Brazil
- 166 Universidad Sergio Arboleda, 11022 Bogotá, Colombia
- 167 University of Minnesota Duluth, Duluth, MN 55812, USA
- 168 Boston University, Boston, MA 02215, USA
- 169 Fluminense Federal University, 9 Icaraí Niterói - RJ, 24220-900, Brazil
- 170 University of California Berkeley, Berkeley, CA 94720, USA
- 171 University of Warsaw, 02-093 Warsaw, Poland
- 172 Indian Institute of Technology Kanpur, Uttar Pradesh 208016, India
- 173 University of Puerto Rico, Mayaguez 00681, Puerto Rico, USA
- 174 Chung-Ang University, Seoul 06974, South Korea
- 175 York University, Toronto M3J 1P3, Canada
- 176 High Energy Accelerator Research Organization (KEK), Ibaraki, 305-0801, Japan
- 177 Yale University, New Haven, CT 06520, USA
- 178 Sanford Underground Research Facility, Lead, SD, 57754, USA
- 179 Rice University, Houston, TX 77005
- 180 Dordt University, Sioux Center, IA 51250, USA
- 181 Iwate University, Morioka, Iwate 020-8551, Japan
- 182 University of Albany, SUNY, Albany, NY 12222, USA
- 183 Jackson State University, Jackson, MS 39217, USA
- 184 University of Novi Sad, 21102 Novi Sad, Serbia
- 185 Erciyes University, Kayseri, Turkey
- 186 Jawaharlal Nehru University, New Delhi 110067, India
- 187 University of Texas at Austin, Austin, TX 78712, USA
- 188 Università degli Studi di Milano, I-20133 Milano, Italy
- 189 Hong Kong University of Science and Technology, Kowloon, Hong Kong, China
- 190 Instituto Tecnológico de Aeronáutica, Sao Jose dos Campos, Brazil
- 191 University of Athens, Zografou GR 157 84, Greece
- 192 Università degli Studi di Pavia, 27100 Pavia PV, Italy
- 193 University of South Carolina, Columbia, SC 29208, USA
- 194 Pennsylvania State University, University Park, PA 16802, USA
- 195 Centro de Investigación y de Estudios Avanzados del Instituto Politécnico Nacional (Cinvestav), Mexico City, Mexico
- 196 Universidade Federal do ABC, Santo André - SP, 09210-580, Brazil
- 197 Eötvös Loránd University, 1053 Budapest, Hungary
- 198 University of Lucknow, Uttar Pradesh 226007, India
- 199 Comisión Nacional de Investigación y Desarrollo Aeroespacial, Lima, Peru
- 200 Istituto Nazionale di Fisica Nucleare, Sezione di Torino, Turin, Italy
- 201 Centro de Tecnologia da Informacao Renato Archer, Amarais - Campinas, SP - CEP 13069-901
- 202 Gran Sasso Science Institute, L'Aquila, Italy
- 203 University of Arizona, Tucson, AZ 85721, USA
- 204 Punjab Agricultural University, Ludhiana 141004, India
- 205 Jeonbuk National University, Jeonrabuk-do 54896, South Korea
- 206 Central University of South Bihar, Gaya, 824236, India
- 207 Universidad Nacional Mayor de San Marcos, Lima, Peru
- 208 Institute of Particle and Nuclear Physics of the Faculty of Mathematics and Physics of the Charles University, 180 00 Prague 8, Czech Republic
- 209 National Institute of Science Education and Research (NISER), Odisha 752050, India
- 210 Texas A&M University - Corpus Christi, Corpus Christi, TX 78412, USA
- 211 University of Medellín, Medellín, 050026 Colombia
- 212 Idaho State University, Pocatello, ID 83209, USA

- 213 Jyväskylä University, FI-40014 Jyväskylä, Finland
 214 Kavli Institute for the Physics and Mathematics of the Universe, Kashiwa, Chiba 277-8583, Japan
 215 Laboratori Nazionali del Gran Sasso, L'Aquila AQ, Italy
 216 University of California Los Angeles, Los Angeles, CA 90095, USA
 217 Institute of High Energy Physics, Chinese Academy of Sciences, Beijing, China

Abstract: The 2x2 Demonstrator, a prototype for the Deep Underground Neutrino Experiment (DUNE) liquid argon (LAr) Near Detector, was exposed to the Neutrinos from the Main Injector (NuMI) neutrino beam at Fermi National Accelerator Laboratory (Fermilab). This detector prototypes a new modular design for a liquid argon time-projection chamber (LArTPC), comprised of a two-by-two array of four modules, each further segmented into two optically-isolated LArTPCs. The 2x2 Demonstrator features a number of pioneering technologies, including a low-profile resistive field shell to establish drift fields, native 3D ionization pixelated imaging, and a high-coverage dielectric light readout system. The 2.4 tonne active mass detector is flanked upstream and downstream by supplemental solid-scintillator tracking planes, repurposed from the MINERvA experiment, which track ionizing particles exiting the argon volume. The antineutrino beam data collected by the detector over a 4.5 day period in 2024 include over 30,000 neutrino interactions in the LAr active volume—the first neutrino interactions reported by a DUNE detector prototype. During its physics-quality run, the 2x2 Demonstrator operated at a nominal drift field of 500 V/cm and maintained good LAr purity, with a stable electron lifetime of approximately 1.25 ms. This paper describes the detector and supporting systems, summarizes the installation and commissioning, and presents the initial validation of collected NuMI beam and off-beam self-triggers. In addition, it highlights observed interactions in the detector volume, including candidate muon anti-neutrino events.

1. Introduction

The Deep Underground Neutrino Experiment (DUNE) [1] is an accelerator-based neutrino observatory currently under construction along the new Long-Baseline Neutrino Facility (LBNF) neutrino beam [2]. DUNE will unambiguously determine the neutrino mass ordering; it will also measure the charge-parity (CP)-violating phase and several neutrino mixing parameters with high precision. Additionally, DUNE will search for physics beyond the Standard Model and utilize any supernova neutrino bursts that occur in its lifetime to study the astrophysics of stellar collapse and the properties of neutrinos [3]. DUNE is composed of a Near Detector (ND) complex located at Fermilab in Batavia, Illinois and a Far Detector (FD) complex positioned 1,285 km away at Sanford Lab in Lead, South Dakota. More information about the experiment and its physics goals can be found in Ref. [1,4].

The FD complex will be constructed in two phases, with Phase I consisting of two, 10 kilo-tonne¹ LArTPCs and an addition of two more detectors available in Phase II. The ND complex [5] will house three detectors situated 574 m downstream of the LBNF neutrino source in a cavern with approximately 60 m of rock overburden. To minimize systemic uncertainties for the oscillation analyses, it is essential to include a LAr target in the ND complex. ND-LAr, a LArTPC based near detector, satisfies this requirement. Together with The Muon Spectrometer (TMS), a magnetized scintillator detector located directly downstream along the beamline, ND-LAr will have the capability of moving orthogonally to the beam axis in order to characterize the LBNF neutrino flux over a range of angles, a technique referred to as PRISM [5]. The third detector in the ND complex, System for

¹ 10 kt of fiducial mass within the instrumented regions, with each cryostat holding a total of 17.1 kt LAr [5]

on-Axis Neutrino Detection (SAND), will remain fixed to characterize and monitor the on-axis beam continuously.

The LBNF beam, currently under construction and slated to become the highest-intensity neutrino beam in the world, will present new challenges for LArTPC neutrino detectors. During Phase I, with LBNF in forward horn current mode, ND-LAr expects an average of 25 neutrino interactions on argon alongside $O(100)$ background events per $9.6\ \mu\text{s}$ beam spill; however, its detector design must also accommodate an increased neutrino interaction rate following the planned Phase II LBNF beam upgrades. To meet DUNE physics requirements, the ND-LAr design has been developed to mitigate interaction pileup in its uniquely high signal-occupancy environment. It features a pixelated charge readout that produces 3D ionization distributions to which reconstruction algorithms can be directly applied; this charge readout works in tandem with a fast (nanosecond-level), high-coverage light readout system within a modular detector design. The modularity of ND-LAr ensures the correct association of charge and light signals for accurate event reconstruction and energy deposition estimation.

A staged prototyping program has been implemented to facilitate the success of the innovative ND-LAr design. The 2x2 Demonstrator represents the first multi-module stage of testing for the fully integrated system, consisting of four prototype modules running in the high-occupancy NuMI beam at Fermilab [6,7]. Each module is approximately 60% of the full-scale design in each transverse dimension and 40% of the height compared to the planned ND-LAr modules. Prior to their installation in the 2x2, each module was tested individually at the University of Bern in Switzerland [8]. The 2x2 Demonstrator sees a neutrino interaction rate per TPC that is comparable to that of ND-LAr, providing a valuable test of the novel detector geometries and technologies devised to mitigate event pileup.

This paper covers the details of, and motivation for, the 2x2 Demonstrator systems' design in Section 2. Section 3 describes the procedures for the installation and commissioning of the detector and cryogenic systems. Section 4 reports on the initial detector performance based on raw data; it includes beam and self-triggering timing validations, as well as visually identified, triggered events.

2. 2x2 Demonstrator Design

This section will summarize the considerations and challenges driving the 2x2 Demonstrator design. It will also describe the detector system layout as a whole, including cryogenic support systems and the NuMI beam configuration.

2.1. LArTPC Detectors: Advantages and Challenges

Since their first large-scale implementation in the early 2000s [9], LArTPCs have furnished the physics community with high-granularity imaging and precise calorimetry in a dense, scalable, uniform, and fully-active detector medium. In conjunction with its high density ($\rho = 1.4\ \text{g/cm}^3$), LAr provides high ionization and scintillation yields of $O(10^4)$ photons and electrons per deposited MeV [10,11], enabling excellent ionizing track reconstruction and making it an ideal target material for neutrino detectors.

LArTPC particle detectors such as ArgoNeuT [12], LArIAT [13], ICARUS [14], MicroBooNE [15], SBND [16], and ProtoDUNE-SP [17] have demonstrated that in a volume of liquid argon sufficiently free of electronegative impurities, ionization electrons can be drifted over the order of meters and imaged at mm-scale resolutions [18–22]. The resultant scalability of the LArTPC increases the likelihood of fully containing neutrino interactions within a detector's fiducial volume, improving its calorimetric performance.

Within a LArTPC, energetic, charged particles produce argon excimers, which in turn decay and produce scintillation light; the fast (singlet state) component of this signal, propagating to the boundaries of a detector within nanoseconds of an interaction, provides an efficient t_0 timestamp. The slow (triplet state) component of the scintillation light follows on the order of a μs . In an environment such as the DUNE ND, with tens of neutrino interactions spanning a $9.6\ \mu\text{s}$ window, even the fast components of scintillation signals can experience pileup if multiple signals become indistinguishable in time. Particularly for interactions with final-state particle tracks detached from the interaction vertex, pileup of fast-component light signal risks merging neutrino interactions during event reconstruction, which can bias calorimetric measurements and event classification.

2.2. ND-LAr: Pileup Mitigation

The ND-LAr design emerged from the ArgonCube development program [23], which aimed to improve upon the performance and robustness of the wire-plane LArTPC design through new and developing technologies. Specifically, ND-LAr seeks to minimize pileup-related biases in event reconstruction through TPC modularity.

Precise energy reconstruction and interaction-type classification will depend upon the successful separation of simultaneous events, a goal which requires ND-LAr to diverge from the monolithic LArTPC design and its traditional technologies. In a LArTPC with a maximum drift length of two meters, at a drift field of $500\ \text{V}/\text{cm}$, the maximum drift time will exceed the length of a beam spill by more than two orders of magnitude. This difference in scale between the charge readout and spill windows can lead to pileup of ionization tracks in a multi-interaction beam spill, an effect which scales with a detector's maximum drift length. To mitigate this pileup, rather than constructing one or two monolithic volumes, ND-LAr will be composed of 35 modules in a $7 \times 5 \times 3\ \text{m}$ volume. Each module will be split along the beam axis into two optically-isolated TPCs, resulting in a total of 70 TPCs. The 2x2 Demonstrator prototypes this with four modules, totaling eight optically-isolated TPCs.

ND-LAr modules will collect charge on pixelated sensors, a charge readout technique new to large-scale LArTPCs [24]. The two spatial dimensions defined by the pixelated anode, when combined with the relative timing of pixel hits, provide native 3D imaging of particle tracks within the detector volume before any reconstruction is applied. To complete this structure while also minimizing uninstrumented regions between each TPC, a novel, low-profile field shell and a dielectric light readout system (LRS) have also been designed [25,26]. Segmenting the detector into multiple independently instrumented, optically-isolated regions and including a light readout to supply interaction timing on a scale capable of resolving the beam structure will improve the ability of ND-LAr to accurately reconstruct tens of neutrino interactions within individual beam spills, in spite of backgrounds and the expected pileup rate.

In the DUNE ND complex, TMS is located downstream of ND-LAr to track and characterize muons exiting ND-LAr. For the 2x2 Demonstrator, repurposed MINERvA [27] planes (Mx2) flanking the LArTPC both upstream and downstream in the beam direction provide similar muon tracking and calorimetry. To reconstruct partially contained events, precise timing is required to match energy depositions in ND-LAr to associated depositions in external detectors like TMS. This is especially true in environments with high rates of interaction pileup, when multiple overlapping or proximal particle trajectories could exit the LArTPC in the span of a several microseconds. Event and interaction-level matching between the 2x2 Demonstrator LArTPC and the Mx2 will provide a valuable test of this process.

2.3. 2x2 Demonstrator: Overview

The 2x2 Demonstrator was installed 102 meters underground in Fermilab's MINOS hall, currently home to the NOvA ND [28] and previously home to the MINOS ND [29], ArgoNeuT [12], and MINERvA experiments. The 2x2 Demonstrator is centered on the beam axis, in the same location as the MINOS Near Detector once occupied, see Figure 1. The four 60%-scale prototype ND-LAr modules that make up the 2x2 Demonstrator are

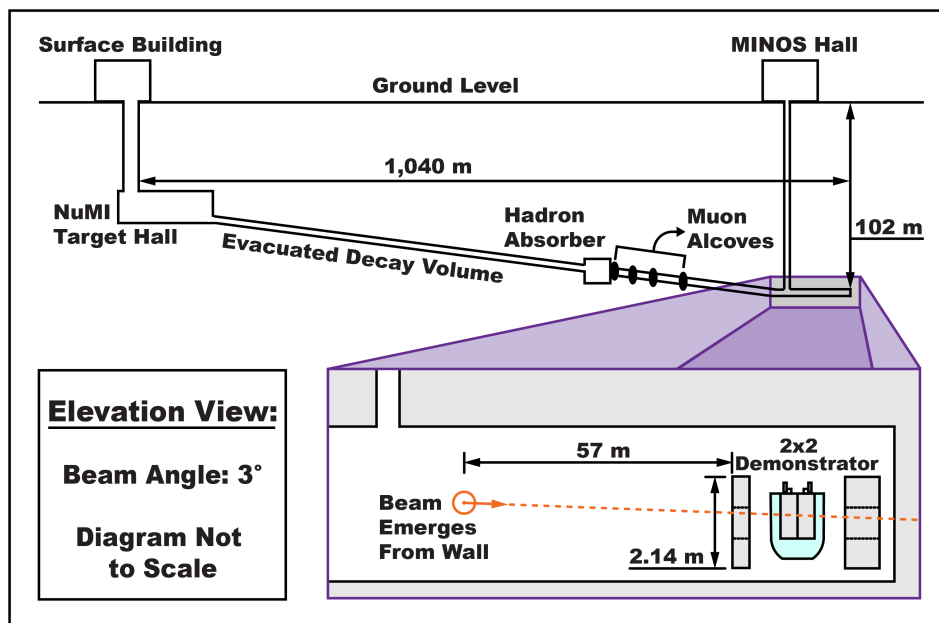


Figure 1. The NuMI Target Hall and Minos Hall, see inset. The 2x2 Demonstrator is located at the downstream end of the MINOS Hall.

suspended in a common bath of liquid argon within a 6.1 m^3 cylindrical, vacuum-jacket insulated cryostat. Together, the four modules form a 2.4-tonne modular LArTPC pictured in Figure 2.

Each module hangs beneath a stainless steel top flange containing five feedthroughs: the detector power and readout cables for each TPC, the high voltage input, detector monitoring and light system calibration inputs, and a LAr fill port. Before insertion into the cryostat, the four modules are connected via a steel cross bar enforcing mm-scale separation between modules. Indium was used to provide a cryogenic seal between the modules, crossbar, and cryostat top plate. The four module units can be seen in Figure 2 prior to their insertion into the cryostat.

Within each module, the two optically-isolated TPCs are instrumented with pixel-based charge readout system (CRS) anodes positioned on either side of a central cathode plane. The light detection systems are located normal to the anode planes on both sides of each TPC; they consist of dielectric, scintillating light traps which provide 29% geometrical coverage within each module.

Located 0.47 meters downstream and 0.75 meters upstream from the cryostat are scintillator-based tracking detectors, which were repurposed from the MINERvA experiment.

2.4. Cryogenic System: Design and Monitoring

Due to the underground location of the 2x2 Demonstrator, direct filling from LAr or N_2 tankers was unfeasible. Consequently, the detector was filled via 160 L dewars lowered by crane into the MINOS Cavern. Throughout operations, LAr purity was maintained through recirculation, with an internal cryogenic centrifugal pump [30] extracting LAr

from the bottom of the cryostat, passing it through O_2 and H_2O filtering media [31,32], and pumping the LAr back into the cryostat through the fill ports positioned at the top of each module. Cooling was provided by three cryocoolers [33], driving cold heads in a LAr condenser. After filling the cryostat, a non-negligible leak was detected along the indium seal joining the modules to the cryostat top plate. A continuous top-up with gaseous argon mitigated the effects of this leak, with H_2O and O_2 gas-getters installed on the input line to preserve LAr purity. Gas analyzers continuously sampled O_2 , N_2 , and H_2O at various locations, including the input and output of the LAr filter.

The cryogenic system was designed to provide 40 mm of dielectric shielding of LAr to the high voltage system. Due to a difference between the as-built detector and the design, the position of the condenser boil-off line limited the maximum dielectric shielding to 20 mm for the duration of the 2024 run. The maintained LAr level served as adequate shielding for the design voltage of 500 V/cm. Following the initial data-taking period in July 2024, the condenser boil-off line was moved, extending the possible voltage range for future runs to 1 kV/cm. A calibrated liquid-level sensor provided input to the high-voltage interlock whenever voltage was applied.

2.5. NuMI Beam

The 2x2 Demonstrator sits 1.04 km downstream of the NuMI target facility at Fermilab. To produce the NuMI beam, 120 GeV protons from Fermilab's Main Injector Accelerator are directed at a 1.2 m graphite target, yielding charged kaons and pions that are subsequently either focused or deflected from the beam path by electromagnetic focusing horns. The beam can run in both neutrino and antineutrino mode, depending upon the polarity of the current supplied to the focusing horns. For the duration of the 2024 run, NuMI ran with reverse horn current (RHC) to produce a muon antineutrino beam.

After the focusing horns, the hadrons produced at the beam target enter a 675 m decay pipe, followed by 240 m of rock. The muon antineutrinos emitted as the hadrons decay in flight have an average energy of 5.8 GeV (see Figure 3). For the medium energy RHC configuration, the NuMI beam is expected to have a high purity of approximately 95% antineutrinos. Figure 1 shows the layout of the beam and injector facilities with respect to the MINOS hall [6].

The Main Injector beam spill spans 9.6 μs , with varying cycle times depending on the configuration of the accelerator complex. Between July 8th and July 12th, when the 2x2 collected physics data, the cycle time between consecutive spills was approximately 1.2 seconds.

2.6. LArTPC Design and Readout

Details of the 2x2 module design are summarized below, and a full description of module hardware can be found in [8]². As the four 2x2 modules were constructed and tested sequentially over several years, hardware upgrades and variations were integrated into the modules. The differences are summarized in Table 1. Modules will be referred to as Module 0, 1, 2, and 3, based on the order in which they were constructed.

The 2x2 modules are housed in 1.4 m tall sleeves of 6 mm thick G10/FR-4 [34], each with a 0.7 m \times 0.7 m footprint. The sleeve's base is left open to facilitate LAr circulation and its top is attached to the cryostat flange [5]. The choice of G10/FR-4 is advantageous as a construction material as it has a radiation length of 19.4 cm and a hadronic interaction

² This is a report on the design and performance of the first 2x2 module, Module 0, built and operated at the University of Bern.

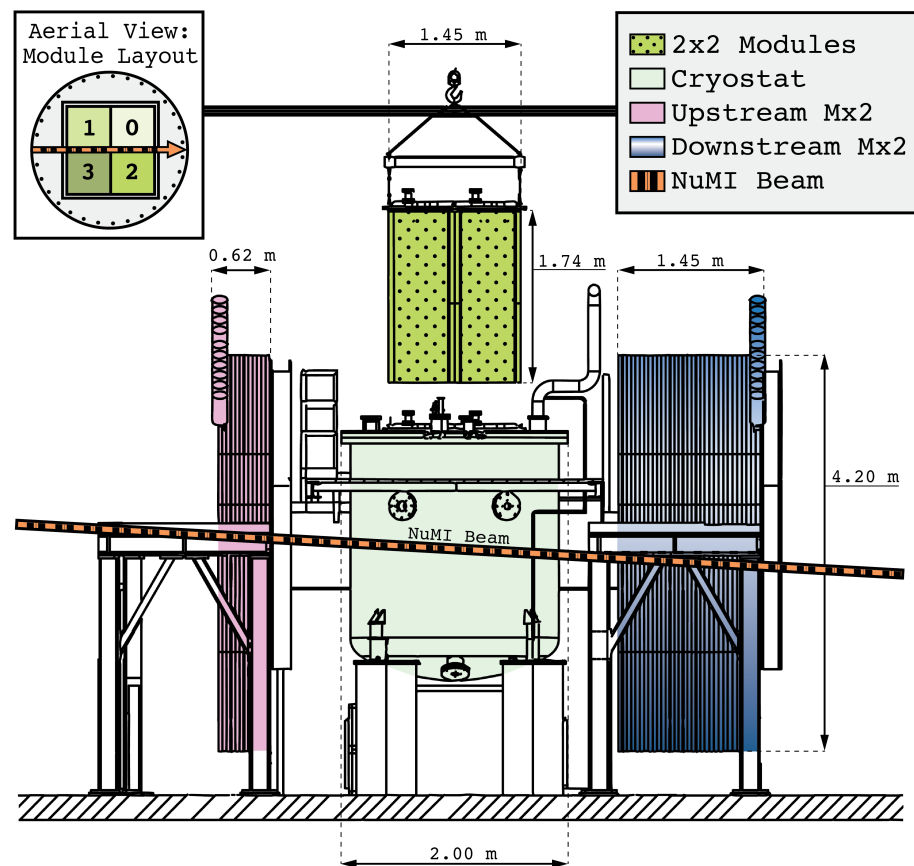


Figure 2. A rendering of the 2x2 Demonstrator and associated systems. The central cryostat contains four independent LArTPC modules in a common bath of liquid argon. Hexagonal steel panels interleaved with scintillator tracking planes, repurposed from the MINERvA detector, are located on both sides of the cryostat, along the axis of the incoming neutrino beam entering from the left.

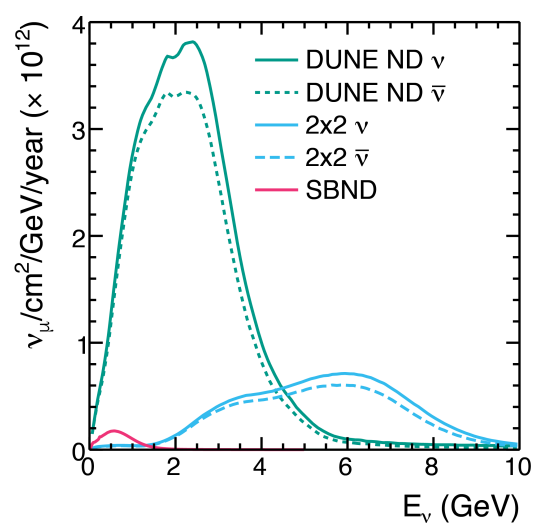


Figure 3. The expected energy and flux of neutrinos from the NuMI beam at the 2x2 Demonstrator, compared to those from the Booster Neutrino Beam (BNB) at the SBN near detector (SBND)[16] and the Phase I LBNF beam at the DUNE ND.

length of 53.1 cm, both of which are on the same scale³ as LAr (14 cm and 85.7 cm, respectively) [36]; this similarity reduces potential event reconstruction complications introduced by the uninstrumented material between fiducial volumes.

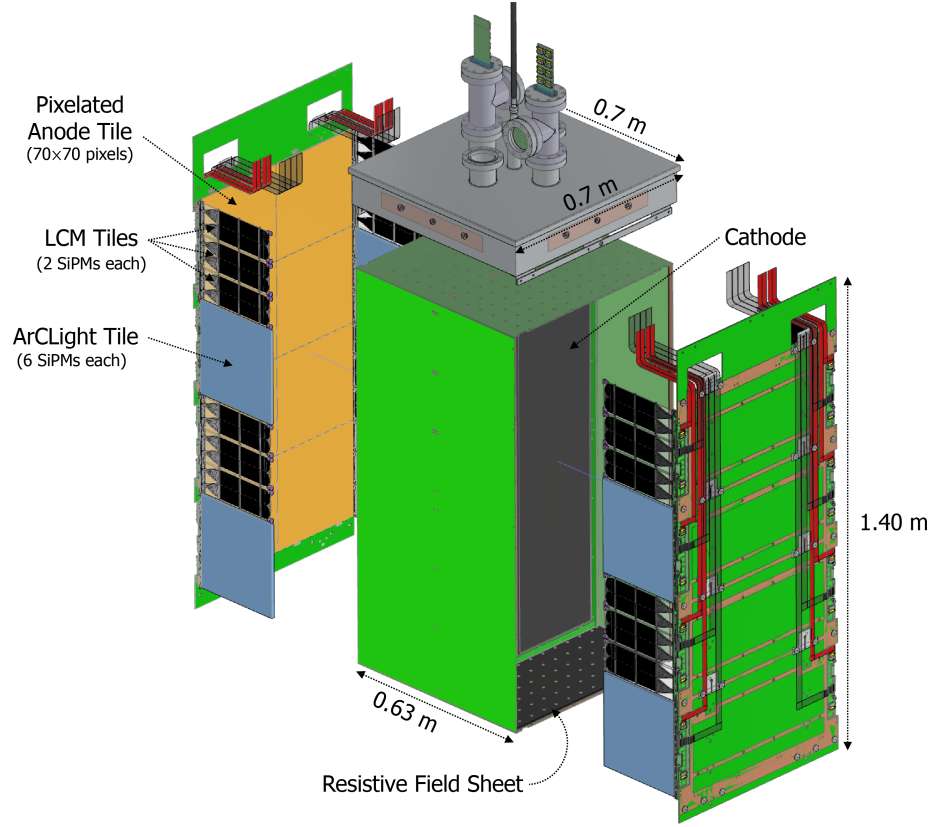


Figure 4. Rendering of a single 2x2 module, as described in [8]. The module is bisected by a resistive cathode to form two optically-isolated LArTPCs. Readout cable positions for the CRS (gray) and LRS (red) can be clearly seen external to the anode, as the external G10 sleeve is not shown.

2.6.1. LArTPC Subsystem: Drift High Voltage

Each 2x2 module is split along the beam axis into two optically-isolated TPC volumes. The maximum drift distance from anode to cathode across each TPC measures 30 cm, requiring only a modest -15 kV potential on the cathode to achieve the nominal field strength of 500 V/cm. This drift high voltage (HV) is supplied for all modules by a Spellman [37] SL50N300/ESL/220 unit. A custom-built oil-filled potted filter-distributor [38] splits the drift HV into four output channels and provides resistive decoupling for the four, while also acting as a low-pass filter for the power supply ripple.

The uniformity of the electric field within each TPC is enforced by a resistive field shell—a departure from the traditional LArTPC resistor-chain field cage. The resistive field shell, constructed from a layer of carbon-loaded Kapton film (DR8) laminated to G10, surrounds each drift region as pictured in Figure 4. At a field strength of 500 V/cm, the 100 μm film has a sheet resistance of $\mathcal{O}(10^9)$ Ω/sq [36]. The field shell is coupled to the anode and cathode by copper cladding; each cathode panel, also constructed from G10/FR-4 and carbon-loaded Kapton film (XC, 25 μm thick), has a reduced sheet resistance of $\mathcal{O}(10^6)$ Ω/sq . Cathodes feature Kapton film on both sides as they bisect the modules [39].

³ For comparison, iron has radiation and hadronic interaction lengths of 1.75 and 16.7 cm, respectively, so a thin G10 shell behaves far more like LAr than a traditional stainless steel field cage [35].

This low-profile field shell design minimizes the uninstrumented material between the instrumented volumes.

2.6.2. LArTPC Subsystem: Charge Readout

Positioned opposite to the central cathode in each module, two anode planes define the outer extent of the mirrored drift regions. Each anode is instrumented by eight large-format, low-profile, printed circuit board LArPix pixel tiles [24]. These are arranged in a 4-high-by-2-wide array, with each individual tile measuring 31 cm \times 32 cm. The LArPix application-specific integrated circuits (ASICs) provide cryogenic-compatible, ultra-low-power amplification, self-triggered digitization, and digital multiplexing for a total of 337,600 pixels in the 2x2 Demonstrator [40]. Each ASIC controls 64 pixel channels, and is packaged to facilitate commercial production and mounted in an array to the back of the anode. Every pixel functions as an independent self-triggering detector and resets with a negligible dead time (approximately 100 ns⁴); consequently, the pixelated readout maintains a manageable data rate and well-resolved tracks even in a high-occupancy environment with multiple events. The raw hit data extracted from each pixel combined with the relative timing of hits across all triggered pixels provide native 3D imaging of particle footprints before any signal processing, filtering, or reconstruction is applied. Timing information from scintillation light detected by the LRS fixes the global position of charge hits in each TPC drift direction. Per TPC, a single on-detector Pixel Array Controller and Network card (PACMAN) unit delivers clean power and establishes I/O with the ASICs, sets configurations, and provides the data acquisition (DAQ) interface for all eight tiles. As mentioned previously, minor prototyping variations between modules are summarized in Table 1.

2.6.3. LArTPC Subsystem: Light Readout

Along the inner face of the vertical field cage panels (normal to the anode plane), eight low-profile, dielectric scintillation light traps span the distance between each anode and the cathode on both sides of the TPC. As mentioned previously, these light traps provide 29% geometrical coverage within each module. Two complementary light trap types alternate along each TPC side, as shown in Figure 4; these are the Light Collection Modules (LCMs) [26] and the ArCLight (ACL) tiles [25,41].

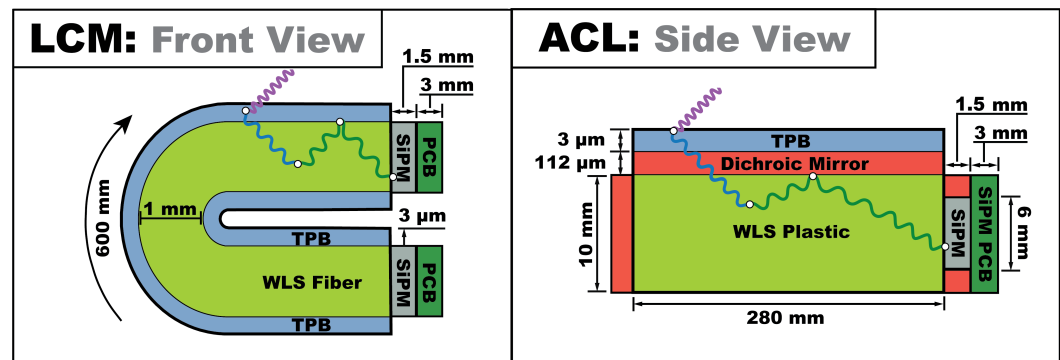
The LCM consists of scintillating fibers coated in tetraphenyl butadiene (TPB) and coupled at each end to silicon photomultipliers [42] (SiPMs). Two SiPMs per LCM are mounted side-by-side with their associated electronics to a 30 cm \times 10 cm \times 0.1 cm PVC backing plate; scintillating fibers are bent, laid flat, and affixed to the same plate such that their ends couple securely to the SiPMs. Within the detector, LCMs are installed in sets of three and occupy an area comparable to that of one ACL. The ACL is a 1-cm-thick plate of wavelength-shifting (WLS) plastic covered by a TPB-coated dichroic mirror foil. In all modules except Module 0, additional strips of dichroic foil prevent light from escaping along the edges of the ACL. A single ACL tile measures 28 cm \times 30 cm \times 1 cm. ACLs are coupled to six SiPMs each [42], for a total of 384 SiPMs in the 2x2 Demonstrator. Schematics of both light trap types are provided in Figure 5.

Signals from the SiPMs undergo pre-amplification on cold electronics, while external variable-gain amplifiers and analog-to-digital converters (ADCs) sample and record the signals at 62.5 MHz with 14-bit resolution. The LRS and CRS both receive a trigger issued

⁴ 100 ns corresponds to an electron traveling 0.16 mm in the detector, given a nominal drift field of 500 V/cm. If a typical pixel hit integrates charge for 2.6 μ s, two back-to-back hits on the same individual pixel separated by a reset would result in a loss of approximately 4% of the second track's charge. This effect impacts tracks traveling perpendicular to the anode, and can be suppressed by alternative LArPix modes.

Table 1. Hardware variations by module.

Feature	Module 0	Module 1	Module 2	Module 3
Pixel Pitch [mm] ^a	4.43	4.43	3.88	4.43
Pixels/Tile	4900	4900	6400	4900
SiPM Model ^b	6025CS	6050CS	6050CS	6050CS
Edge Dichroic Mirror [ACL]	No	Yes	Yes	Yes

^a Distance between the centers of two adjacent pixels^b Hamamatsu S13360**Figure 5.** Schematics of the two LRS light trap types deployed in the 2x2 Demonstrator: the LCM (left) and ACL (right) with their respective dimensions. Installed in the detector, individual LCMs measure 10 cm vertically, while a single ACL spans 30 cm along the same dimension.

in coincidence with the neutrino beam pulse, prompting on-beam readout. Off-beam, every set of six SiPMs triggers independently on an adjustable threshold in order to detect activity like cosmic rays. Blue LEDs located within each TPC, controlled by a custom pulser unit, provide an internal gain calibration source for the individual SiPMs.

Both the ACL and LCM are constructed entirely of dielectric materials and can consequently be placed inside the detector volume without causing significant electric field distortions [8]; this placement optimizes light yield and minimizes the material separating instrumented LAr volumes. LRS design provides a detailed timing structure with vertical spatial resolution. The aim of this design, prototyped in the 2x2 Demonstrator to meet the physics need of ND-LAr, is to mitigate the neutrino interaction pileup expected in a near-beamline detector. In the 2x2 Demonstrator, the TPC maximum drift length defines a charge readout window of approximately 200 μs , while the NuMI beam spill spans only 9.6 μs . As previously mentioned, this order of magnitude difference between the charge readout and spill windows can lead to pileup of ionization tracks from different interactions occurring at different points within a single beam spill. The LRS helps to detangle this pileup: with ACL and LCM light detectors operating on either side of the anode, running along its full vertical length, the LRS achieves sufficient spatial resolution along the vertical and beam-direction axes to define regions of interest within each TPC. Each region is then assigned a timestamp, using timing granularity finer than the NuMI beam bunch structure. The LRS detects individual scintillation signals with nanosecond-level resolution; importantly, this resolution enables the association of daughter particles that are detached from their parent vertices, as in the case of neutral particle decays. By correctly associating ionization charge clusters with significant optical events centered in the same modular region, the ionization signals for each separate neutrino interaction within a spill can be identified and separated in spite of the 200 μs charge readout window.

2.7. Mx2: External Scintillator

Scintillator planes, repurposed from MINERvA, are positioned upstream and downstream of the 2x2 Demonstrator cryostat (see Figure 6), centered along the NuMI beamline. This supplemental system provides tracking for ionizing particles that pierce the LArTPC detector and are particularly useful for charged pion and muon discrimination. The planes are composed of WLS fibers encased in plastic scintillator strips, arranged in 3 orientations with respect to the beam for 3D reconstruction. Three different configurations of scintillator planes are used: tracker planes composed solely of scintillator strips, as well as electromagnetic and hadronic calorimeter planes, interleaved with lead sheets and steel plates, respectively. Figure 7 provides an overview of their composition, and a detailed description can be found in [27].

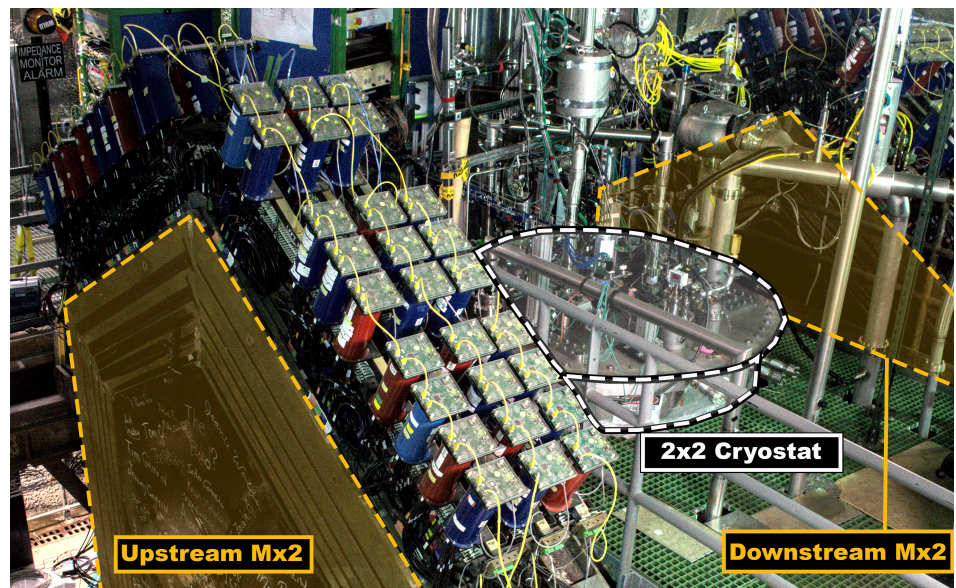


Figure 6. The 2x2 Demonstrator consists of a 2x2 array of modular LArTPCs flanked upstream and downstream by Mx2 scintillating tracker planes.

Between the upstream and downstream components, the Mx2 supplies approximately 5.6 tonnes of active, fiducial scintillator mass, made up of 7.8% hydrogen and 92.2% carbon atoms. The Mx2 has a spatial resolution of 3.1 mm and a timing resolution of 3 ns [27]. The Mx2 reuses readout electronics from MINERvA, including original photomultiplier tubes (PMTs), front-end mother boards, and in-rack custom electronics and power supplies. The DAQ [43], as developed for MINERvA, was reused with minimal changes⁵.

3. Installation and Commissioning

The following section outlines the activities from the initial module construction and cosmic data taking at the University of Bern to the installation of the full 2x2 Demonstrator at Fermilab. This section also describes the commissioning of the 2x2 Demonstrator's cryogenic and detector systems in the lead-up to its run in 2024.

3.1. Module Construction and Installation

Between 2021 and 2023, the 2x2 Demonstrator modules were sequentially constructed and operated at the University of Bern, where they recorded cosmic ray muons in pure

⁵ The Mx2 DAQ triggers on the NuMI A9, a TTL (Transistor-Transistor Logic) early warning signal indicating an incoming beam pulse. This initiates a 216 μ s delay, after which a 16 μ s readout gate is opened on all channels to capture the entire NuMI beam pulse as well as delayed light from decaying particles inside the detector.

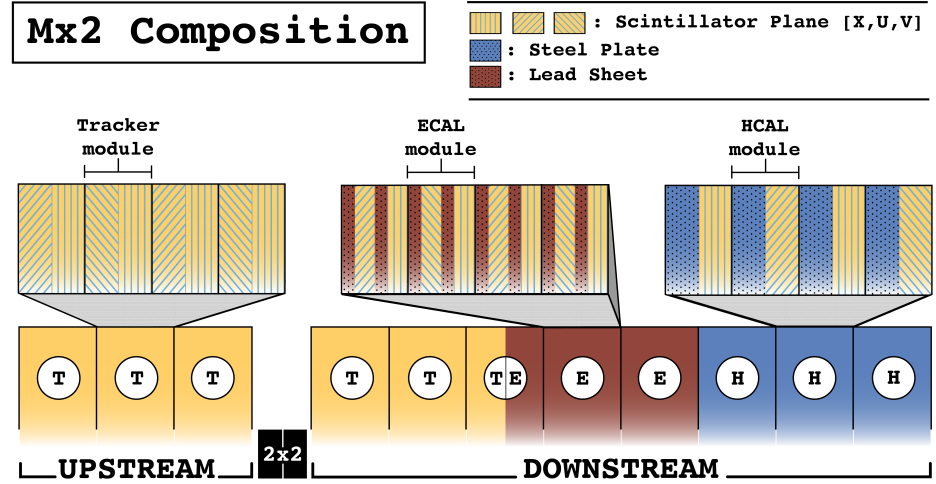


Figure 7. Muon taggers positioned 75 cm upstream and 47 cm downstream of the 2x2 LArTPC consist of three different types of tracking planes. The downstream modules were designed to also perform calorimetric measurements. A total of 185 128-channel multi-anode Hamamatsu H8804 PMTs are mounted atop the Mx2 module sets (one set consisting of four sequential modules); the upstream modules sport 57 PMTs, while the downstream modules operate the remaining 128.

LAr for approximately one week per test run. Details of the assembly and performance of Module 0 were published in [8].

Over the same period, the infrastructure in the MINOS cavern at Fermilab was upgraded in preparation for the 2x2 Demonstrator installation. Both the MINOS and MINERvA experiments were removed from the cavern, while electrical, networking, and environmental safety systems were updated to meet the requirements of the 2x2 Demonstrator. In 2022 and 2023, the cryostat and the Mx2 were installed and their control systems subsequently commissioned.

As the modules completed their individual test runs at the University of Bern, they were shipped fully-assembled to Fermilab and underwent warm acceptance tests on arrival. In October 2023, the four modules were lowered 102 meters by crane into the MINOS cavern. Once underground, they were arranged into a two-module by two-module array and installed in their cryostat, as shown in Figure 8. Installation of the remaining site infrastructure and supporting cryogenics system was completed in March 2024, whereupon the 2x2 Demonstrator subsystems collected warm commissioning data in the NuMI beam for detector calibration. In May 2024, purging of the 2x2 Demonstrator cryostat commenced, and the detector was filled with LAr by May 31st.

3.2. Commissioning: Cryogenics

Leak-checking of the vessel after filling revealed a gaseous argon (GAR) leak in the indium seal joining the modules and the cryostat. This leak necessitated the installation of a continuous GAR top-up system, as well as O₂ and H₂O gas purifiers to minimize adding contaminants from the GAR. Additionally, a malfunctioning component of the detector condenser needed replacement, impacting the system's ability to maintain a high level of LAr purity. Once a spare was acquired, cryogenic commissioning continued. The cryogenic adjustments made in the period following the initial fill corresponded to an electron lifetime of approximately 100 μ s, resulting in a charge loss of $\sim 86\%$ for signals drifted over the full 30 cm anode-to-cathode distance during this initial period of operation.

Between July 5th and July 6th, in a brief window between high voltage runs, new cartridges were installed in the O₂ and H₂O gas-getters. This maintenance period mitigated

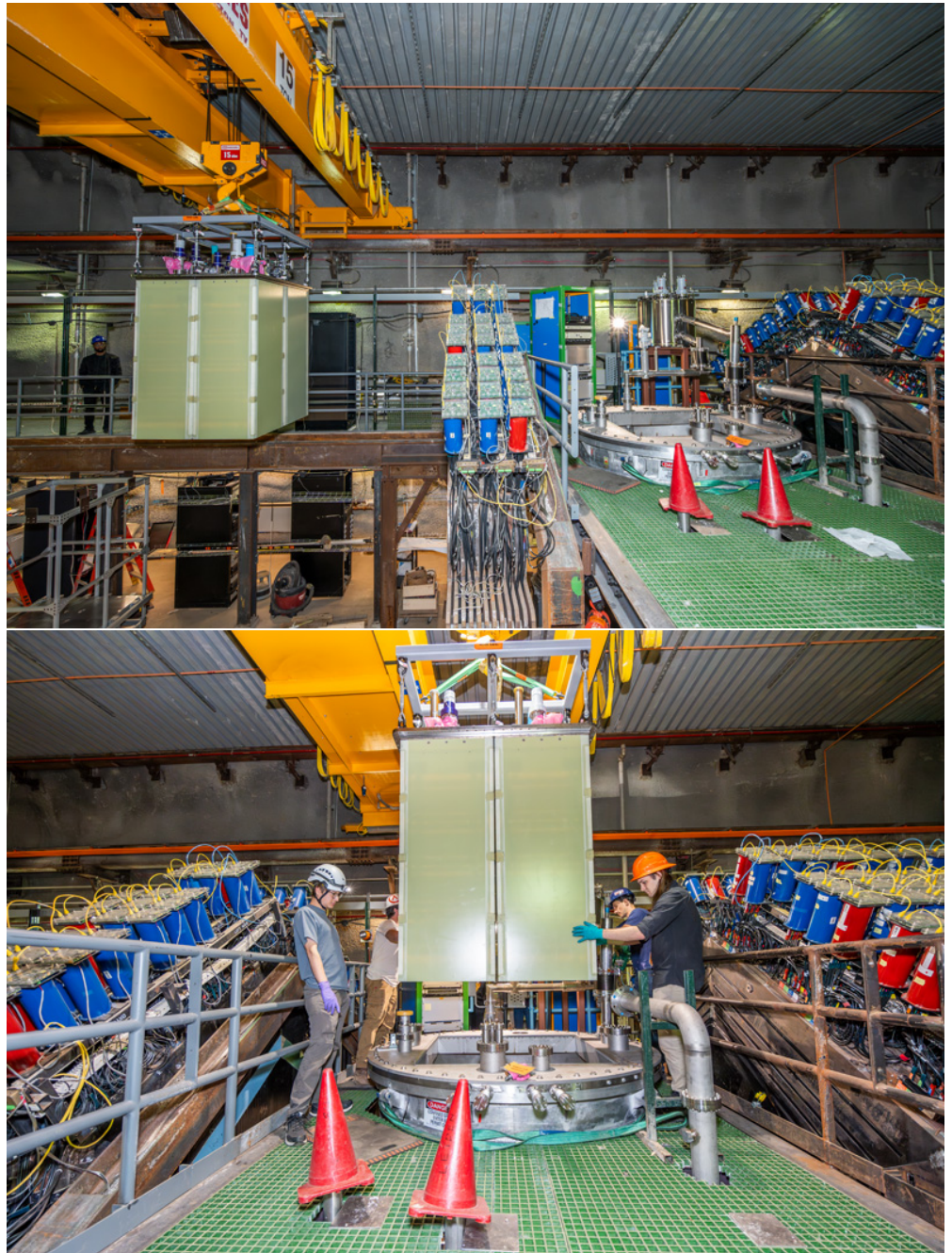


Figure 8. Installation of the 2x2 module array in the MINOS Underground Hall on October 23rd, 2023 [44].

the full-drift charge attenuation to $\sim 15\%$, establishing an improved electron lifetime which remained stable at approximately 1.25 ms for the remainder of the 2024 run.

3.3. Commissioning: TPC High Voltage

During cryogenic commissioning, several cross-checks were performed to verify the successful integration of the HV system. The resistances across the HV feed-throughs were measured, confirming good connections at the cathodes; the potted filter-distributor, system monitoring and controls, and the interlocks were likewise tested.

Cryogenic commissioning completed shortly before the Fermilab Summer Accelerator Shutdown in 2024; consequently, limited time was available for cold commissioning the detector with the HV system fully ramped. The LRS provides HV monitoring during ramps, as potential electric breakdowns will produce flashes of light in the detector. Low cosmic muon rates underground improved the LRS sensitivity to any such flashes relative to the single-module runs at the University of Bern⁶.

On July 1st, the TPC HV system began ramping at a conservative rate of 25 V/s, pausing every 0.5 kV to monitor the status of the TPCs. The detector was held at half-nominal voltage for 12 hours ensure HV stability before completing its ramp to nominal voltage. The aggregate ramp from null to nominal TPC HV took 28.8 hours.

On July 4th, an unintentional cessation of the HV occurred when the liquid-level interlock tripped, providing an opportunity to test the monitoring system's stability and robustness. The system and detector suffered no ill effects due to this HV trip, and cryogenic work leading up to the July 7th ramp significantly improved the LAr purity.

On July 7th and July 8th, the 2x2 Demonstrator was ramped to nominal voltage and ran continuously until midday on July 12th.

3.4. Commissioning: Light Readout

Prior to the conclusion of cryogenic commissioning, the LRS underwent several commissioning stages. In warm conditions, connections along the cold and warm readout chain were tested and confirmed in stages. At this preliminary stage, 13 SiPMs were flagged as non-working or exceeding acceptable noise levels, constituting 3.5% of all LRS channels. Once the cryostat was filled with LAr, the current draw of each cold electronics board was confirmed to lie within the expected range. Between the June 2024 and the July 2024 HV ramps, an ADC unit was replaced due to variable baselines, reducing the number of non-working or noise-dominated channels to 11 (2.8% of the total). The LED settings for each module were tuned for every SiPM and then deployed in automated calibration scripts. Calibration data were then taken at varying SiPM bias voltages, increasing the bias in steps of 0.5 V between each calibration run in order to determine optimal overvoltage settings for each SiPM. The average bias voltage across all operational LRS channels during the 2024 run was 46.8 V, corresponding to an average breakdown voltage of 42.3 V and an overvoltage of 4.5 V. Following this optimization of the LED and SiPM settings, calibration data were once again taken to extract the gain and resolution of each channel. Due to the tight commissioning timeline driven by the beam shutdown, the opportunity for LRS commissioning with the HV on was limited in this initial run.

3.5. Commissioning: Charge Readout

During cryogenic commissioning but before the HV period, the charge readout was commissioned in multiple steps. First, a communication network between the ASICs of

⁶ A trial ramp to half-nominal (250 V/cm) field strength was performed to commission the system after the detector was initially filled on May 31st. During the May 31st trial ramp, slight deviations from nominal light rates were observed in the 2x2 Demonstrator. Offline investigations concluded that the elevated rates were due to low LAr purity rather than complications within the HV system.

each pixel tile was established. At this stage, 43 out of 6400 ASICs were disabled due to unreliable communication or recurring bit-corruption issues. Next, a measurement of the baseline offset was performed by periodically sampling the charge on every pixel: this check quantifies the pedestal for each readout channel, and higher baseline noise in specific regions of the detector helps identify sources of noise impacting the charge readout. Once pedestals were quantified, the channel-level thresholds for the nominal self-triggering operations were tuned such that the trigger rate on each channel lay between 0.01 and 0.1 Hz. The total fraction of disabled channels following this commissioning stage was 2.25%. Finally, estimate the threshold values, a special run was carried out where the periodic reset of the front end, typically configured with a period of 10-100 μ s, was disabled such that the slowly integrating charge from leakage currents induced at-thresholds triggers. The obtained thresholds were found to be 5 k electrons on average.

3.6. Data Collection: Nominal HV with LAr Purity

The 2x2 Demonstrator collected 86 hrs of NuMI beam data at nominal running conditions, with a field strength of 500 V/cm and a high level of LAr purity ($\mathcal{O}(\text{ms})$). Additional data taken at half-nominal field strength completes the physics data set, bringing the total run time with beam and high LAr purity to 4.5 days. This period of 100% detector up-time corresponded to 1.5×10^{19} protons on target (POT), which produced more than 30k (anti)neutrino interactions in the LArTPC volume. A summary of the detector status and corresponding NuMI beam configuration is shown in Figure 9. Throughout the run, the Mx2 and LRS triggered on NuMI A9 early-warning signals to capture beam spills, while the LRS additionally triggered on off-beam interactions exceeding a set light threshold. The CRS pixels self-triggered continuously on independent, pixel-by-pixel thresholds; additional markers in the CRS data stream tagged NuMI A9 and LRS threshold triggers to assist in event building during downstream processing. Six hours of additional, low-threshold, non-beam data were collected for charge readout commissioning studies on July 12th, 2024, after which the detector ramped down for further cryogenic improvements.

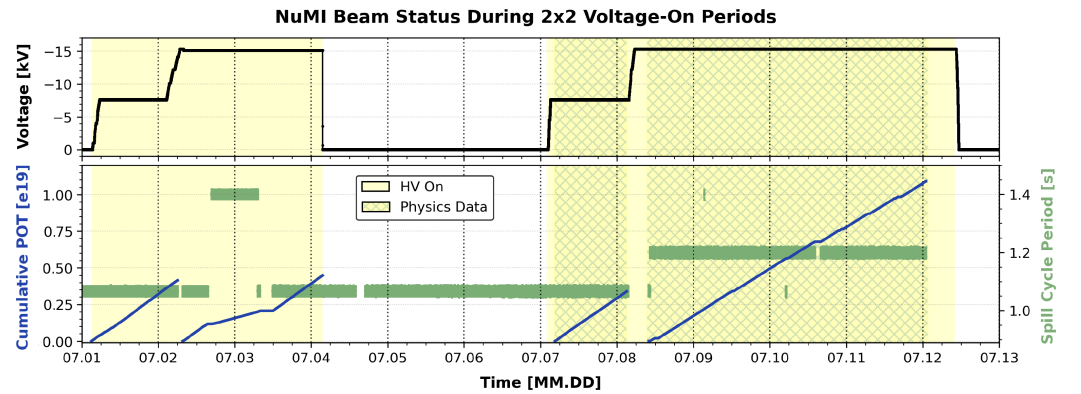


Figure 9. Recorded POT for the NuMI beam by the 2x2 Demonstrator (blue). The green line indicates when the beam was running and shows the cycle of the beam pulses delivered. The topmost panel shows the TPC HV applied to the 2x2 cathode(s) in black.

4. Data Validation and Event Displays

The innovative technology prototyped in the 2x2 Demonstrator—namely its native 3D pixelated charge readout—coupled with a low background, underground environment enables instantaneous proof of detector performance and the viability of the ND-LAr design. During the 4.5-day physics-quality run, LArTPC events could be viewed in event displays like those shown at the end of Section 4 almost immediately, using minimally processed

raw data. The 2x2 Demonstrator collaboration will publish data analyses utilizing offline event reconstruction at a later date. The remainder of this paper focuses on validations of trigger synchronization between detector subsystems and the NuMI beam, as well as event displays demonstrating the performance of the 2x2 Demonstrator with minimally processed data.

4.1. Validation: Multi-Detector Triggering

The three detector subsystems (LRS, CRS, and Mx2) record data through distinct DAQs in separate data streams. The event-level trigger alignment of each subsystem with the NuMI beam A9 early warning signal, as well as each subsystem's timing offsets relative to each other, must be well understood. A validation of the detector's trigger alignment is essential to ensure accurate offline data matching and event reconstruction.

Within the LArTPC, the charge readout and the light readout share a common on-beam triggering system. The light readout warm electronics receive the NuMI A9 directly and trigger, then forward the signal to a PACMAN controller to tag the spill window in the self-triggering charge readout. Mx2, in contrast, triggers independently, but also on the NuMI A9.

In order to optimize timing measurements within the 2x2 Demonstrator LArTPCs, the LRS has been configured to record light waveforms over a period of $16\ \mu\text{s}$. Each trigger is padded by approximately $1.6\ \mu\text{s}$ prior to beam arrival, and the LRS continues taking data for several μs following the spill period to ensure full coverage of any associated secondary interactions or decays. The Mx2 likewise pads its beam window by a period of $0.5\ \mu\text{s}$ and collects data for $5.5\ \mu\text{s}$ following the end of the spill.

Figure 10 shows the integrated and normalized data rate spanning two hours from the three detector subsystems (CRS, LRS and Mx2) relative to the arrival of the beam pulse. When compared to Figure 11, in which the 6-batch structure of the NuMI beam is visible, it is evident that all three subsystems successfully trigger on the beam. The beam structure is apparent in the shape of the Mx2 integrated waveforms and, to a lesser degree, in the light readout integrated waveforms.

4.2. Validation: Charge Readout Self-triggering

One advantageous feature of the 2x2 Demonstrator charge readout is its ability to self-trigger on events without reliance on an external beam or light threshold triggers. Outside of the $\sim 0.8\ \text{Hz}$ NuMI beam spills, most high-energy interactions in the 2x2 Demonstrator stem from muons, often minimally ionizing, produced by cosmic ray interactions in the atmosphere. The MINOS ND, when located where the 2x2 Demonstrator currently stands, measured a cosmic muon rate of $27\ \text{Hz}$ [45]. Although the MINOS target and the 2x2 target are materially different, the rock overburden is unchanged, so a scintillating detector with an approximate volume of $2\ \text{m}^3$ is estimated to detect cosmic muon events at a rate of around $2\ \text{Hz}$. Figure 12 shows the self-trigger data rates for the charge readout system over several seconds, along with the t_0 of NuMI beam triggers. A clear correlation can be observed between self-triggered hits from the pixelated charge readout and the beam signal from NuMI. In addition, the non beam-correlated spikes are consistent with the rate of cosmic muons expected in the 2x2 ($\sim 2\ \text{Hz}$).

4.3. Visual Confirmation of Neutrino Interactions

With minimal offline processing, data recorded within a NuMI beam trigger can be visually analyzed to confirm the presence of neutrino interactions and the validity of the detector systems.

The 2x2 Demonstrator expects two consistent sources of relatively high-energy background events. The first, mentioned previously, are cosmic muons. These have no correla-

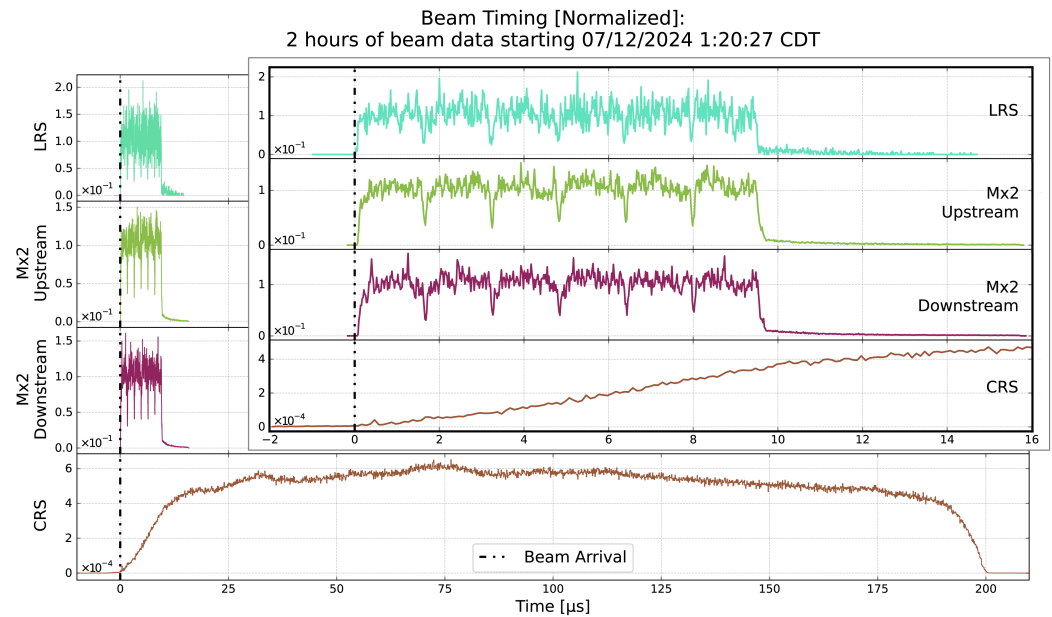


Figure 10. The maximum readout window of a single beam spill in the 2x2, 200 μs , is defined by the maximum drift time for charge. Above, the recorded signal outputs of the three subsystems of the 2x2 (LRS, Mx2, and the CRS), summed across two hours of beam spills, are plotted against the maximum readout window. Focusing on the first 16 μs (see inset), the successful alignment between subsystems is evidenced by the nearly simultaneous arrival time of beam signal. Note that the LRS and Mx2 pad their readout by different lengths of time before and after the beam arrival, as determined by each systems' respective DAQ requirements.

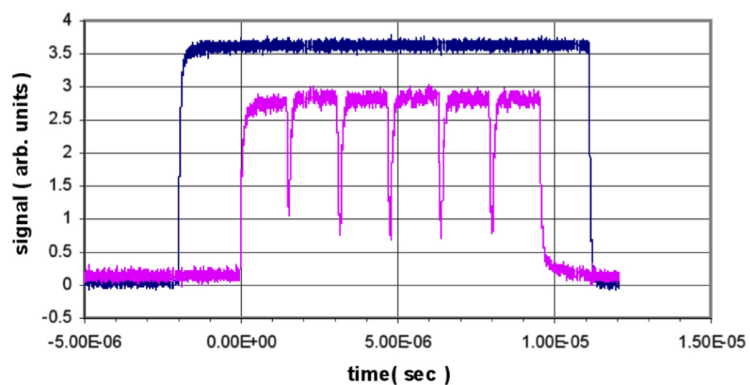


Figure 11. In magenta: the NuMI beam structure is evident in the NuMI toroid signal, with the beam running in slip-stacked, NuMI-only mode. In dark blue: NuMI's beam trigger window [6].

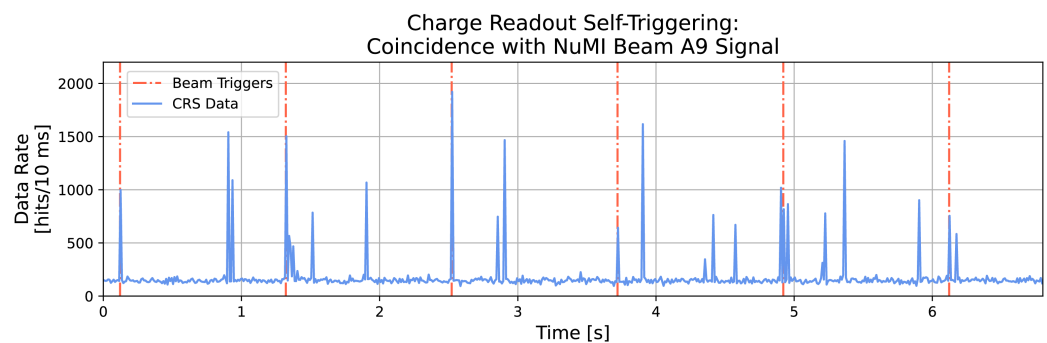


Figure 12. CRS self-trigger hit rates (blue) as a function of time, overlaid with A9 triggers from the NuMI beam (orange) indicating beam spill arrival times.

tion to the beam timing. Due to the short duration of the NuMI beam pulse and the beam's comparatively long cycle time, beam events without any cosmic background are common. The second background source are muons produced by NuMI beam neutrino interactions in the rock between the beam target and the detector hall, called rock muons. These ionizing particles coincide with the beam spill. Simulations of rock muon interactions in the nearest 100 meters of rock to the 2x2 Demonstrator suggest that an average of one to three rock muons will pass through the 2x2 LArTPC or its Mx2 muon-tagging planes during each beam pulse. Preliminary visual scanning of beam data supports this approximation, and a more detailed analysis is in progress.

The first events presented below, Events 1 and 2, were selected from our high-purity, beam-on dataset via visual scanning. These events feature data from all three subsystems. The data from the LArTPCs have not yet undergone full offline reconstruction; only minimal calibration has been applied to the raw data products. In each display, multiple charged current interactions occur in the LArTPC detector volume across one beam spill; these neutrino interactions are accompanied by multiple rock muon tracks visible in the external Mx2 planes, some of which enter the LArTPC. This density of events, while less than that expected at ND-LAr, provides an excellent test of the high-coverage LRS, the pixelated CRS, and the efficacy of detector modularity in separating simultaneous interactions.

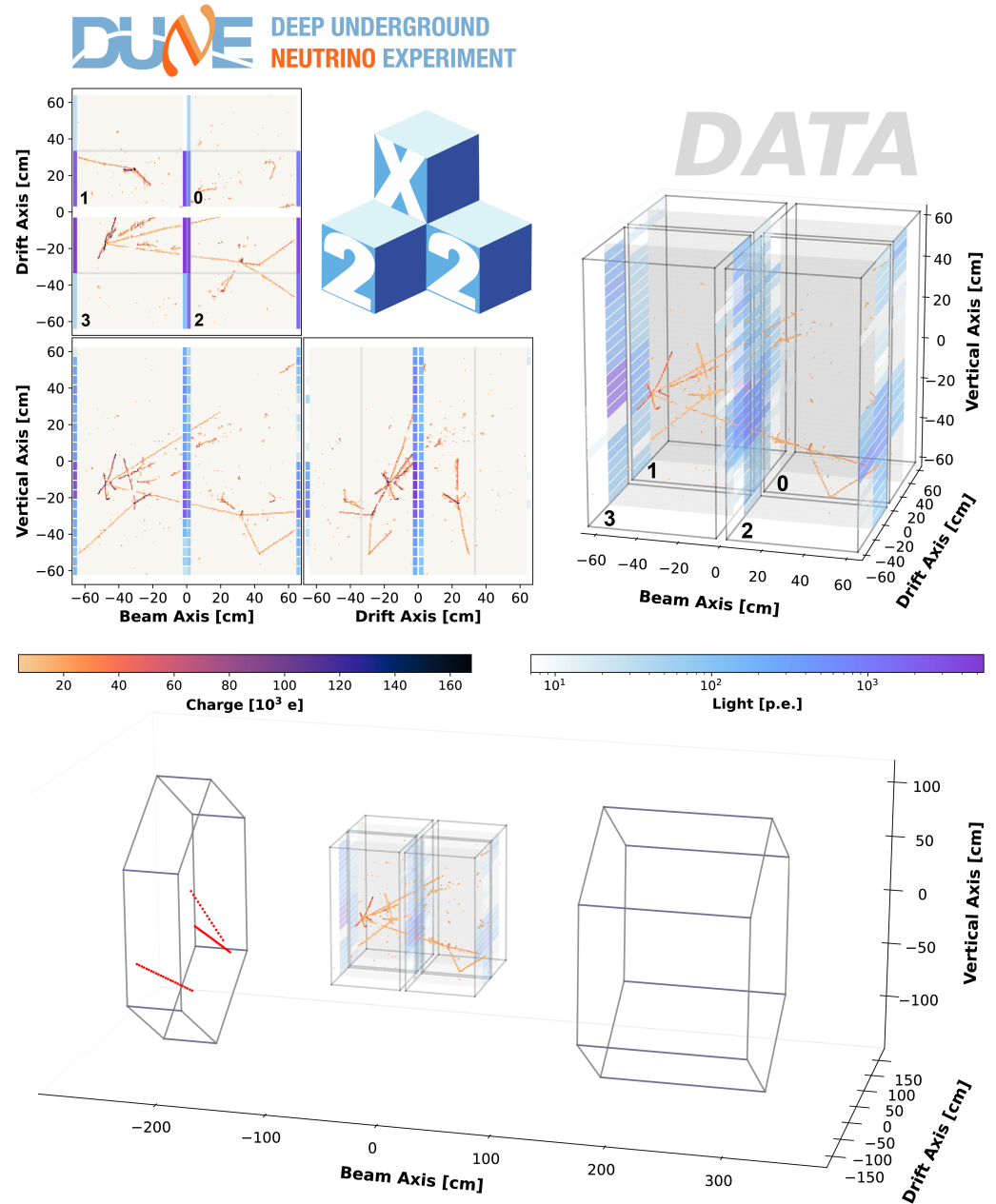
Also included is an event display of a beam spill in which only rock muons deposited energy in the detector volume (Event 3), as well as a cosmic muon event recorded between beam spills (Event 4). These event displays provide insight into two prominent background topologies for both the 2x2 Demonstrator and ND-LAr.

The event displays included in this paper feature a 3D projection of CRS and LRS data; an additional 3D projection includes particle trajectories passing through the upstream and downstream Mx2 planes when appropriate. Light waveforms have been corrected for baseline offsets, and SiPM responses have been equalized and converted from ADC counts to detected photoelectrons using the calibrations reported in Section 3. The following event displays use calibrated light data to render ACL and LCM responses visually coherent. Given the impracticality of displaying full light waveforms from all 384 SiPMs, the calibrated sum of each SiPM waveform is represented in the 3D projections as a colored panel. The colored panels extend along the drift axis to cumulatively fill the geometric area occupied by TPB-coated, ACL or LCM light traps within the detector. Although multiple SiPMs are coupled to each light trap, each SiPM sum is displayed independently to better demonstrate the systems' capability for spatial discrimination.

Also included are 2D projections of both the charge and light signals for each event. Three projections—one from above the detector, one side-on along the beam axis, and the last side-on along the drift axis—show charge and light signal summed along the third, flattened axis. Light signal sums are represented by colored rectangles running along the borders of each TPC. These rectangles do not extend along the drift axis in the side-on projection in order to avoid obscuring the charge data.

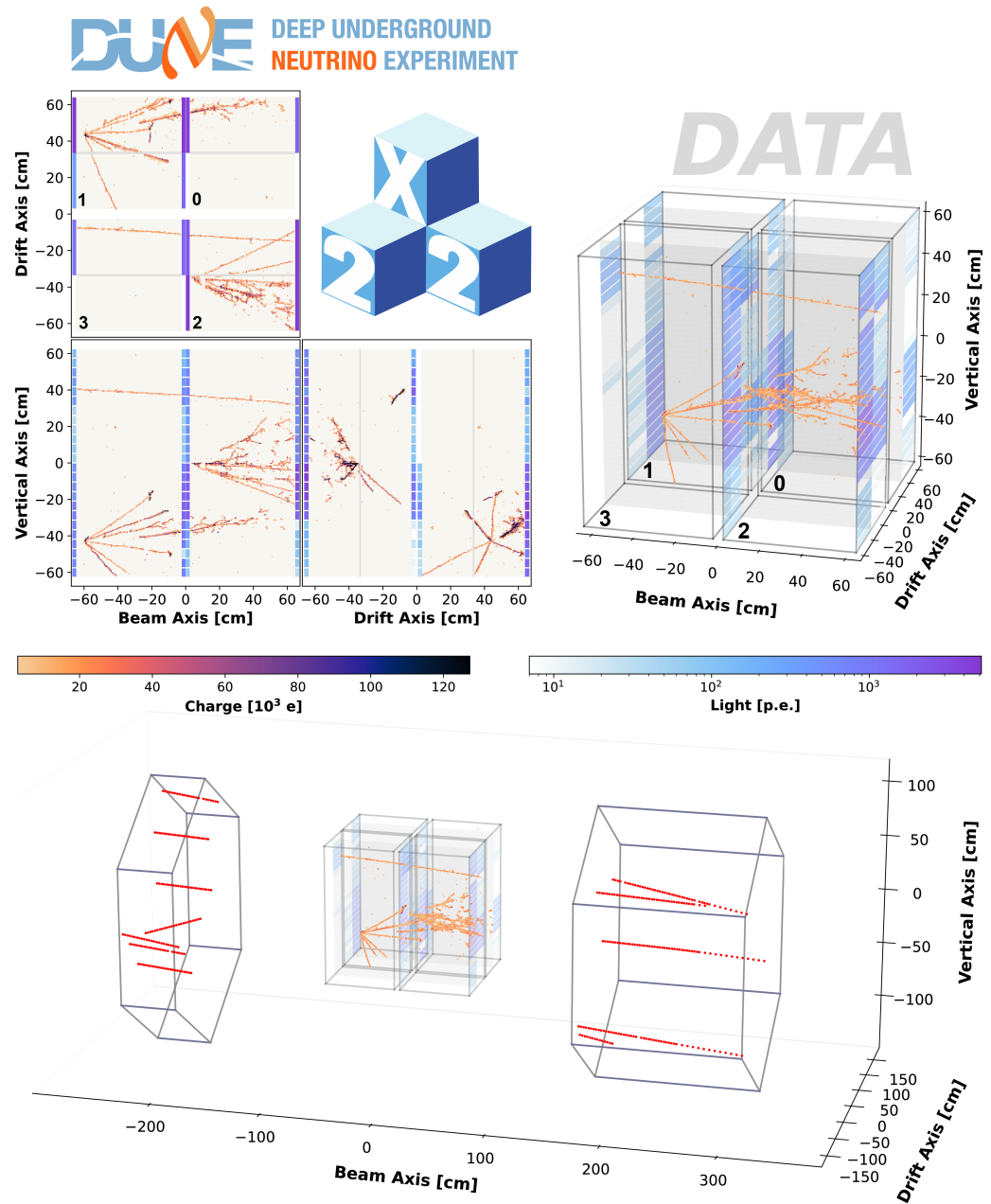
Event 1: NuMI beam trigger on contained charged current muon neutrino

This event shows a charged current neutrino interaction with its vertex in Module 3, upstream. The interaction produces one through-going muon track which passes above the downstream Mx2 planes, as well as several other tracks that are contained within the LArTPC volume.



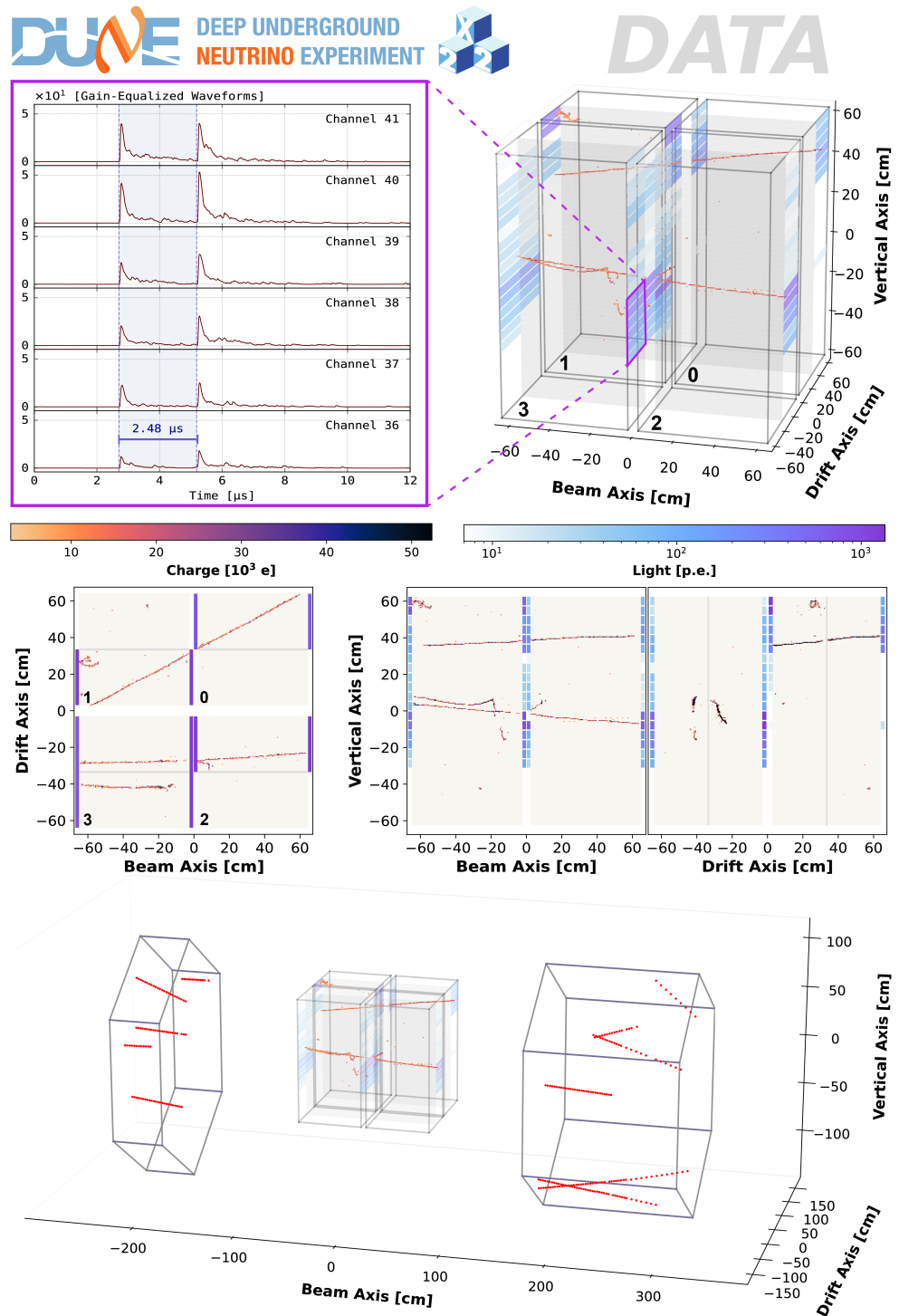
Event 2: NuMI beam trigger on two charged current neutrino interactions

Two charged current neutrino interactions, one in Module 1 and the other in Module 2, produce tracks within the LArTPC volume. A rock muon passing through both upstream and downstream Mx2 taggers pierces Modules 2 and 3 during the same period of $16\ \mu\text{s}$, but the neutrino interactions remain well separated from each other by the detector's modularity.



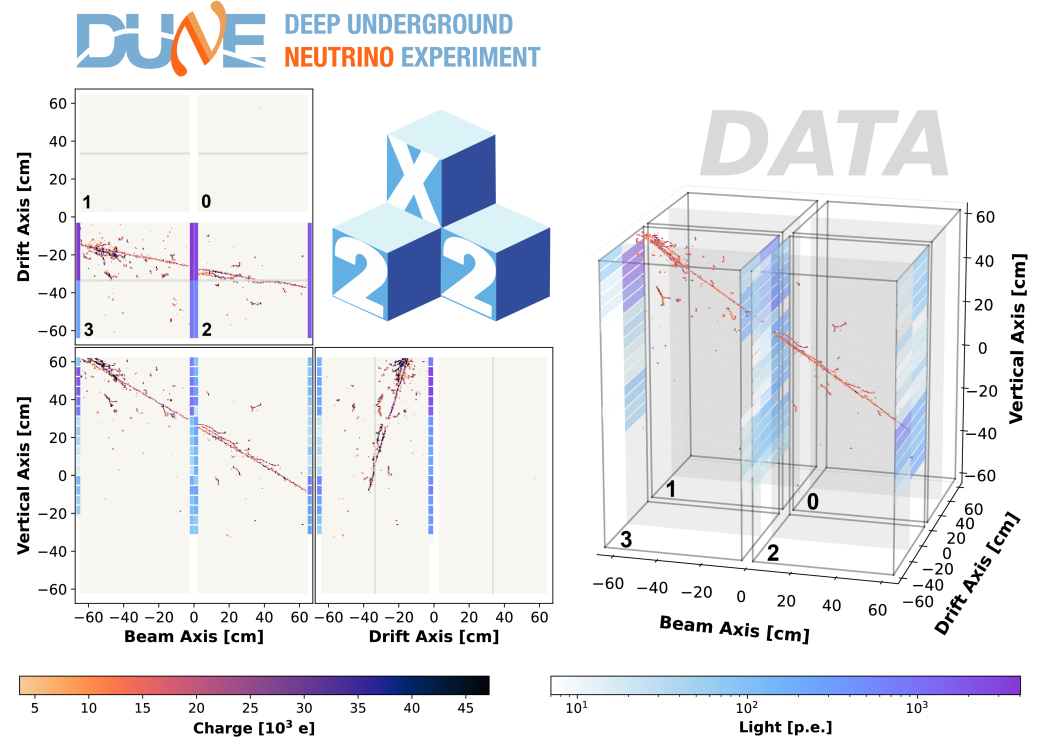
Event 3: NuMI beam trigger on external neutrino interactions with Michel electron

Several rock muons produce tracks in the LArTPC volume; one of these muons decays in Module 3, generating a Michel electron. In the light waveforms corresponding to the LCMs nearest the decay (top left), one can see a separation of $2.48 \mu\text{s}$ between fast scintillation signals associated with the muon and the Michel electron.



Event 4: Light threshold trigger on cosmic muon

A cosmic muon enters the LArTPC at a relatively shallow angle: with only the prompt pixel hits, showering tracks are clearly defined, while the y-axis spatial resolution of the LRS is visible in the waveform sums bordering each charge display. Additionally, as the cosmic muon only deposits energy in Modules 2 and 3, the successful optical isolation of adjacent TPCs is clearly demonstrated. As the external Mx2 panels trigger solely on the NuMI A9 early-warning signal, there are no recorded Mx2 tracks corresponding to this off-beam LArTPC event.



5. Lessons Learned

The 2x2 Demonstrator, as an intermediate stage in the ND-LAr prototyping process, has informed updates to the intended ND-LAr design. Several of these updates have already been tested in the Full Scale Demonstrator (FSD), a single ND-LAr-scale module assembled and run at the University of Bern. The FSD was successfully operated at a nominal drift field of 500 V/cm during October and November 2024. The FSD prototyped shielding on the LRS cold electronics, which improved the isolation between the charge and light subsystems. It also featured updated warm and cold cabling for the LRS, as well as a new iteration of the pixelated anode tiles. These alterations reduced the noise levels observed in the LArTPC data, particularly for the LRS. Although the resistive field shell described in Section 2 was successfully prototyped in the 2x2, cost constraints motivated its replacement by an equally low-profile resistor-chain field shell. This design was successfully operated in 2024 as part of the FSD, and its performance satisfies ND-LAr physics requirements. Future testing in the 2x2 Demonstrator and the FSD will aim to streamline calibration methods, further reduce noise levels, and improve the dynamic range of the LRS. Additionally, the Module Row Prototype, still under construction at Fermilab, will test the mounting, structural support, and installation of five full-scale modules ahead of ND-LAr assembly.

6. Conclusions

Between June 11th and July 12th 2024, the 2x2 Demonstrator of the DUNE Near Detector LArTPC was commissioned and collected 10 days of on-axis NuMI beam data at Fermilab. Of the collected data, 86 hrs of the NuMI triggered beam data were collected at nominal running conditions, with a field strength of 500 V/cm and a LAr purity of approximately 1.25 ms. In total, the 2x2 Demonstrator is expected to have collected over 30,000 neutrino interactions. Although data collected by the 2x2 Demonstrator will be processed through customized reconstruction [46,47] and analysis tools, the clarity of event topologies in the July 2024 dataset enable us to identify and display the first recorded neutrino events in a DUNE prototype detector using minimally-processed subsystem signal data.

The 2x2 Demonstrator is expected to resume collecting neutrino data when the NuMI beam returns. In the interim, the existing dataset is being utilized as a training tool for upcoming analyses. In addition, these data will help to advance the development of native 3D reconstruction algorithms, to validate the proposed design of the DUNE Near Detector, and to inform the development of future LArTPC detectors.

7. Acknowledgments

This document was prepared by the DUNE collaboration using the resources of the Fermi National Accelerator Laboratory (Fermilab), a U.S. Department of Energy, Office of Science, HEP User Facility. Fermilab is managed by Fermi Forward Discovery Group, LLC, acting under Contract No. 89243024CSC000002. This work was supported by CNPq, FAPERJ, FAPEG and FAPESP, Brazil; CFI, IPP and NSERC, Canada; CERN; MŠMT, Czech Republic; ERDF, H2020-EU and MSCA, European Union; CNRS/IN2P3 and CEA, France; INFN, Italy; FCT, Portugal; NRF, South Korea; CAM, Fundación “La Caixa”, Junta de Andalucía-FEDER, MICINN, and Xunta de Galicia, Spain; SERI and SNSF, Switzerland; TÜBİTAK, Turkey; The Royal Society and UKRI/STFC, United Kingdom; DOE and NSF, United States of America. This research used resources of the National Energy Research Scientific Computing Center (NERSC), a U.S. Department of Energy Office of Science User Facility operated under Contract No. DE-AC02-05CH11231.

This manuscript has been authored by Fermi Forward Discovery Group, LLC under Contract No. 89243024CSC000002 with the U.S. Department of Energy, Office of Science, Office of High Energy Physics.

1. Abud, A.A.; et al. Deep Underground Neutrino Experiment (DUNE), Far Detector Technical Design Report, Volume II: DUNE Physics, 2020, [arXiv:hep-ex/2002.03005].
2. Strait, J.; et al. Long-Baseline Neutrino Facility (LBNF) and Deep Underground Neutrino Experiment (DUNE) Conceptual Design Report Volume 3: Long-Baseline Neutrino Facility for DUNE June 24, 2015, 2016, [arXiv:physics.ins-det/1601.05823].
3. Abud, A.A.; et al. Supernova neutrino burst detection with the Deep Underground Neutrino Experiment: DUNE Collaboration. *The European Physical Journal C* **2021**, *81*. <https://doi.org/10.1140/epjc/s10052-021-09166-w>.
4. Abi, B.; et al. Deep Underground Neutrino Experiment (DUNE), Far Detector Technical Design Report, Volume I Introduction to DUNE. *JINST* **2020**, *15*, T08008, [arXiv:physics.ins-det/2002.02967]. <https://doi.org/10.1088/1748-0221/15/08/T08008>.
5. Abud, A.A.; et al. Deep Underground Neutrino Experiment (DUNE) Near Detector Conceptual Design Report, 2021, [arXiv:physics.ins-det/2103.13910].
6. Adamson, P.; et al. The NuMI neutrino beam. *Nuclear Instruments and Methods in Physics Research Section A: Accelerators, Spectrometers, Detectors and Associated Equipment* **2016**, *806*, 279–306. <https://doi.org/10.1016/j.nima.2015.08.063>.

7. Ainsworth, R.; et al. An Upgrade Path for the Fermilab Accelerator Complex, 2022, [arXiv:physics.acc-ph/2106.02133].
8. Abud, A.; et al. Performance of a Modular Ton-Scale Pixel-Readout Liquid Argon Time Projection Chamber. *Instruments* **2024**, *8*, 41, [arXiv:physics.ins-det/2403.03212]. <https://doi.org/10.3390/instruments8030041>.
9. Arneodo, F. The ICARUS Experiment, A Second-Generation Proton Decay Experiment and Neutrino Observatory at the Gran Sasso Laboratory, 2001, [arXiv:hep-ex/hep-ex/0103008].
10. Miyajima, M.; et al. Average energy expended per ion pair in liquid argon. *Phys. Rev. A* **1974**, *9*, 1438–1443. <https://doi.org/10.1103/PhysRevA.9.1438>.
11. Doke, T.; et al. Absolute Scintillation Yields in Liquid Argon and Xenon for Various Particles. *Japanese Journal of Applied Physics* **2002**, *41*, 1538. <https://doi.org/10.1143/JJAP.41.1538>.
12. Anderson, C.; et al. The ArgoNeuT detector in the NuMI low-energy beam line at Fermilab. *Journal of Instrumentation* **2012**, *7*, P10019–P10019. <https://doi.org/10.1088/1748-0221/7/10/p10019>.
13. Acciarri, R.; et al. The Liquid Argon In A Testbeam (LArLAT) experiment. *Journal of Instrumentation* **2020**, *15*, P04026–P04026. <https://doi.org/10.1088/1748-0221/15/04/p04026>.
14. Amerio, S.; et al. Design, construction and tests of the ICARUS T600 detector. *Nuclear Instruments and Methods in Physics Research Section A: Accelerators, Spectrometers, Detectors and Associated Equipment* **2004**, *527*, 329–410. <https://doi.org/https://doi.org/10.1016/j.nima.2004.02.044>.
15. Fleming, B. The MicroBooNE Technical Design Report, 2012. <https://doi.org/10.2172/1333130>.
16. Nebot-Guinot, M. Status of the Short-Baseline Near Detector at Fermilab. *Phys. Sci. Forum* **2023**, *8*, 22. <https://doi.org/10.3390/psf2023008022>.
17. Abud, A.A.; et al. Design, construction and operation of the ProtoDUNE-SP Liquid Argon TPC. *Journal of Instrumentation* **2022**, *17*, P01005. <https://doi.org/10.1088/1748-0221/17/01/P01005>.
18. Abratenko, P.; et al. Search for an Excess of Electron Neutrino Interactions in MicroBooNE Using Multiple Final-State Topologies. *Phys. Rev. Lett.* **2022**, *128*, 241801, [arXiv:hep-ex/2110.14054]. <https://doi.org/10.1103/PhysRevLett.128.241801>.
19. Acciarri, R.; et al. Design and construction of the MicroBooNE detector. *Journal of Instrumentation* **2017**, *12*, P02017–P02017. <https://doi.org/10.1088/1748-0221/12/02/p02017>.
20. Abi, B.; et al. First results on ProtoDUNE-SP liquid argon time projection chamber performance from a beam test at the CERN Neutrino Platform. *JINST* **2020**, *15*, P12004, [arXiv:physics.ins-det/2007.06722]. <https://doi.org/10.1088/1748-0221/15/12/P12004>.
21. Cicerchia, M. Study of cosmic rays in the ICARUS-T600 detectors. *PoS* **2024**, *TAUP2023*, 165. <https://doi.org/10.22323/1.441.0165>.
22. Acciarri, R.; et al. First measurement of electron neutrino scattering cross section on argon. *Physical Review D* **2020**, *102*. <https://doi.org/10.1103/physrevd.102.011101>.
23. Amsler, C.; et al. ArgonCube: a novel, fully-modular approach for the realization of large-mass liquid argon TPC neutrino detectors. Technical report, CERN, Geneva, 2015.
24. Dwyer, D.; et al. LArPix: demonstration of low-power 3D pixelated charge readout for liquid argon time projection chambers. *Journal of Instrumentation* **2018**, *13*, P10007–P10007. <https://doi.org/10.1088/1748-0221/13/10/p10007>.
25. Gauch, A.; et al. Scintillation light detection performance for the DUNE ND-LAr 2 × 2 modules. *Journal of Instrumentation* **2023**, *18*, C04004. <https://doi.org/10.1088/1748-0221/18/04/C04004>.
26. Anfimov, N.; et al. Development of the Light Collection Module for the Liquid Argon Time Projection Chamber (LArTPC). *Journal of Instrumentation* **2020**, *15*, C07022. <https://doi.org/10.1088/1748-0221/15/07/C07022>.
27. Aliaga, L.; et al. Design, calibration, and performance of the MINERvA detector. *Nuclear Instruments and Methods in Physics Research Section A: Accelerators, Spectrometers, Detectors and Associated Equipment* **2014**, *743*, 130–159. <https://doi.org/10.1016/j.nima.2013.12.053>.
28. Habig, A. The NOvA Experiment. *Nuclear Physics B - Proceedings Supplements* **2012**, 229–232, 460. Neutrino 2010, <https://doi.org/https://doi.org/10.1016/j.nuclphysbps.2012.09.097>.
29. Michael, D.G.; et al. Observation of Muon Neutrino Disappearance with the MINOS Detectors and the NuMI Neutrino Beam. *Phys. Rev. Lett.* **2006**, *97*, 191801, [hep-ex/0607088]. <https://doi.org/10.1103/PhysRevLett.97.191801>.

30. Barber Nichols. *Installation, Operation and Maintenance Manual BNHeP-36-000 Liquid Helium Pump and Liquid Argon Pump*.
31. Research Catalysts, Inc. *Material Safety Data Sheet (MSDS) for Q-5 Copper Catalyst*.
32. ThermoFisher Scientific. *Molecular Sieves 4A, 8 to 12 Mesh*.
33. Cryomech. *AL600 Gifford-McMahon Cryocooler*.
34. Curbell Plastics. *About G10/FR-4 Glass Epoxy*.
35. Particle Data Group. Atomic and nuclear properties of iron (Fe). https://pdg.lbl.gov/2024/AtomicNuclearProperties/HTML/iron_Fe.html, 2025. Accessed: 2025-05-13.
36. Auger, M.; et al. A New Concept for Kilotonne Scale Liquid Argon Time Projection Chambers, 2019, [arXiv:physics.ins-det/1908.10956].
37. Spellman High Voltage Electronics Corporation. *SL 10W to 1200W Compact HV Power Source*.
38. Shell Diala. *Safety Data Sheet, Shell Diala S2 ZX-A*.
39. Berner, R.; et al. First Operation of a Resistive Shell Liquid Argon Time Projection Chamber: A New Approach to Electric-Field Shaping. *Instruments* **2019**, *3*, 28, [arXiv:physics.ins-det/1903.11858]. <https://doi.org/10.3390/instruments3020028>.
40. Russell, B. The 2x2 Demonstrator - A demonstrator for the DUNE ND-LAr Near Detector based on the ArgonCube Design. *PoS* **2024**, *TAUP2023*, 221. <https://doi.org/10.22323/1.441.0221>.
41. Bürgi, J.; et al. Improvement and Characterisation of the ArCLight Large-Area Dielectric Light Detector for Liquid-Argon Time Projection Chambers. *Instruments* **2024**, *8*. <https://doi.org/10.3390/instruments8040048>.
42. Hamamatsu. *MPPC S13360 Series Datasheet*.
43. Perdue, G.; et al. The MINERvA data acquisition system and infrastructure. *Nuclear Instruments and Methods in Physics Research Section A: Accelerators, Spectrometers, Detectors and Associated Equipment* **2012**, *694*, 179–192. <https://doi.org/10.1016/j.nima.2012.08.024>.
44. Svoboda, D. Fermilab Visual Media: The 2x2 prototype detector for the DUNE near detector was placed in its cryostat, 2024. Photograph. Accessed: 2024-08-01.
45. Adamson, P.; et al. Observation of seasonal variation of atmospheric multiple-muon events in the MINOS Near and Far Detectors. *Physical Review D* **2015**, *91*. <https://doi.org/10.1103/physrevd.91.112006>.
46. Acciarri, R.; et al. The Pandora multi-algorithm approach to automated pattern recognition of cosmic-ray muon and neutrino events in the MicroBooNE detector. *Eur. Phys. J. C* **2018**, *78*, 82, [arXiv:hep-ex/1708.03135]. <https://doi.org/10.1140/epjc/s10052-017-5481-6>.
47. Dominé, L.; et al. Point proposal network for reconstructing 3D particle endpoints with subpixel precision in liquid argon time projection chambers. *Phys. Rev. D* **2021**, *104*, 032004, [arXiv:hep-ex/2006.14745]. <https://doi.org/10.1103/PhysRevD.104.032004>.